ORIGINAL ARTICLE
Journal Section

Contextual learning improves forest aboveground biomass estimates from UAV-LiDAR: use of tree height associations

Jaime C. Revenga[1] | Stefan Oehmcke[2] | Mana Gharun[3] | Flurin Sutter[4] | Fabian Gieseke[2] | Katerina Trepekli[1] | Nina Buchmann[5] | Alexander Damm[6,7]

[1]Institute of Geosciences and Natural Resources Management (IGN), Copenhagen University, Denmark
[2]Institute of Computer Science (DIKU), Copenhagen University, Denmark
[3]Institute of Landscape Ecology, Biosphere-Atmosphere Interaction, University of Münster, Germany
[4]Swiss Federal Institute for Forest, Snow and Landscape Research (WSL), Forest Dynamics Research Unit, Switzerland
[5]Department of Environmental Systems Science, ETH Zürich, Switzerland
[6]Department of Geography, University of Zürich, Winterthurerstrasse 190, 8057 Zurich, Switzerland
[7]Eawag, Swiss Federal Institute of Aquatic Science & Technology, Surface Waters – Research and Management, Ueberlandstrasse 133, 8600 Duebendorf, Switzerland

Correspondence
Jaime C. Revenga, Institute of Geosciences and Natural Resources Management (IGN), Copenhagen University, 1350, Copenhagen, Denmark
Email: jar@ign.ku.dk

Forest structure analysis and biomass prediction systems are key tools for advancing forest trait-based ecology. Surveys using Unmanned Aerial Vehicles (UAV) and Light Detection and Ranging (LiDAR) systems have contributed to this field with increased accuracy in tree phenotyping. Moreover, methods combining UAV-LiDAR surveying and machine learning (ML) have also emerged to enhance estimates of single tree traits. Here, we utilized a UAV-LiDAR system to survey a Norway spruce forest in Davos, Switzerland, where a detailed field-based inventory served as ground truth data. Our objectives were (i) to gain insights into variation and gradients of tree height and (ii) to evaluate whether such insights may prove useful as contextual information to improve predictions of stem diameter and tree-level biomass. We segmented the point cloud data scene into individual canopies and treated the LiDAR-derived tree height as the variable of interest. We then used local indicators of spatial association to detect the significant local context, and defined tree neighborhoods within the forest. Then, we extracted metrics from the neighborhoods and introduced them in a ML regression experiment to evaluate predictions of individual tree diameter. The focus was on comparing performance of tree diameter predictions between regression models that either consider neighborhood metrics (i.e. context-aware models), or not. Next, AGB was estimated from the tree height derived from the UAV-LiDAR survey, the predicted tree diameter and allometry. The benefits of context awareness were assessed in terms of accuracy gained in estimating AGB. We obtained results of different machine learning methods (i.e. AdaBoost, Lasso and Random Forest) and evaluated these based on nested cross-validation. We applied this approach to two separate tree data sets within the same site, one being clustered and continuous, the other discontinuous and scattered in separate sampling plots. In both cases, we found evidence of enhanced AGB prediction performance in context-aware regressions, where the RMSE was reduced by 4.0% and by 9.1%, respectively. These findings indicate that gradients in tree heights across the ecosystem may proxy for local microclimate, edaphic conditions and biotic factors that influence tree growth, which can be leveraged to enhance predictions of AGB. The method proposed is fully native to UAV-LiDAR data.

KEYWORDS

aboveground biomass, contextual learning, forest structure, functional trait mapping, machine learning, quantitative ecology, UAV-LiDAR

1 | INTRODUCTION

Forest aboveground biomass (AGB) is an important component for determining global land carbon (C) budgets. Worldwide, the role of forests is considered essential to understand the exchange of C between the atmosphere and biosphere [1, 2], and a large body of environmental remote sensing (RS) research has advanced our understanding of it. However, current assessments of C-cycling in forest ecosystems present uncertainties, and contrasting findings exist [3], partly caused by the limited accuracy of AGB estimates [4, 5]. This underscores the need for new, transparent and transferable methods to advance quantitative estimates of AGB [6].

Traditionally, predictive analyses in forest research and phenotyping from RS data have focused on regressions considering only individual tree attributes as predictors (e.g. tree height, canopy metrics) [7, 8] and fitted allometric models [9], disregarding the influence of neighboring trees on the response variable. Such tree-level analyses have been crucial to improve the characterization of e.g. optical vegetation traits [10], tree dendrometry [11], or species composition [12]. However, these approaches do not account for the influence of the spatial context on the individual tree trait under investigation, be it abiotic factors (e.g. terrain condition, soil depth) or biotic interactions (e.g., light interception, nutrient competition). Over time, methods using information of neighboring trees to enhance individual tree trait regressions (i.e. metrics derived from monitoring inventory plots) have been proposed, such as non-linear mixed effects (NLME) methods [13, 14, 15], or competition-based methods [16, 17, 18]. This line of research has shown that the neighborhood information matters, and its positive impact has been documented in various tree-level regression analyses, e.g. productivity [19, 20], fuel potential [21] or diverse structural metrics [15, 22, 23].

However, despite the utility of current methods that leverage neighborhood metrics such as tree stand information, from a RS perspective they remain unsatisfactory in some respects. Many of such methods are not directly transferable to a RS framework because they use understory metrics as predictors, which are difficult to survey reliably from an above-canopy perspective [16, 17]. Remarkably, questions remain about the optimal scale at which such neighborhood metrics become relevant and therefore should be retrieved [19, 20]. However, a common procedure is considering the trees contained in an arbitrarily delineated inventory plot, whose size is defined to fit management or monitoring purposes [20]. This approach poses the shortcoming of neglecting the spatial scale at which relevant ecological phenomena operate (e.g. the appropriate range at which competition effects are significant), so the analysis remains constrained by the effects of the plot size [13, 14, 15, 16, 17]. To the best of our knowledge, tree-level AGB and trait assessments considering neighborhood information are currently limited due to one or more of the following reasons: (i) they characterize the spatial context with uniquely process-specific indices (e.g. competition pressure from immediate neighbors) [16, 17, 18]; (ii) they calibrate models with neighborhood-metrics retrieved from artificially-bounded inventory plots (e.g. NLME methods) [13, 14, 15]; or (iii) they do not sufficiently account for the spatial scale at which an ecological phenomenon affects the trait under investigation. Moreover, when the relationship between the plot-level predictors used and any ecological phenomenon is described, often ancillary data sources are incorporated (e.g. tree stand age) [17, 24] or poorly quantified forest management metrics, e.g. "stand quality", "site index", "dominance index" [14, 17, 24]. These shortcomings are constrained by the specific data collection protocol, and currently hinder transferring such methods to an integrated RS framework, which would allow conducting standardized and replicable forest analyses in other regions and at larger scales.

From a technical pespective, Unstaffed Aerial Vehicles (UAV) equipped with Light Detection and Ranging (LiDAR) monitoring systems are regarded as particularly versatile [25], accurate and cost-effective tools [26] to contribute to the task of extensive phenotyping, bridging scales in AGB mapping, particularly covering the scale between *in situ* field-based inventories (ca. 0-1 ha) and airborne LiDAR datasets (ca. 0-10^4 km^2) [27, 28]. With a surveying accuracy comparable to field-based measurements, UAV-LiDAR monitoring provides datasets (i.e. point cloud data, PCD) that allow individual tree phenotyping at an intermediate spatial scale (1-40 ha). The combination of flexibility and accuracy of UAV-LiDAR systems enables quantitative phenotyping of single trees across the landscape (e.g. inspection of tree heights across an environmental gradient), providing extensive and accurate datasets that facilitate analyses at the tree level [7].

While both theoretical and technological advances have accelerated the progress of forest AGB research in an unprecedented manner, there is still room for improvement as regards integrating ecological reasoning into AGB research. For instance, it is commonly argued that understanding local ecological processes requires monitoring biomass of individual trees [17, 19, 20, 29]. However, the opposite idea is seldom discussed: how and to what extent can community ecology processes be harnessed in tree-level AGB regression experiments? [16, 18] We consider this line of work within AGB research as yet relatively unexplored, with some exceptions. Earlier works have proposed to account for the effects of immediate competition pressure on tree growth with either distance-based [18] or distance-independent metrics [16, 30], and judge such approaches beneficial to improve regression results. For instance, Sun et al. (2019) [16] evaluated the potential of distance-independent and ranking-based tree competition indices to predict tree diameter growth, and found them outperforming competition-unaware prediction models. Similarly, Zhang et al. (2020) [17] ranked trees by competition levels and applied a quantile regression model to enhance predictions of the height-to-diameter ratio.

In this scenario, nonparametric ML regression methods seem a sound approach to incorporating a contextual analysis, given that they are flexible and have successfully been integrated into RS forest mapping studies [31]. Such context-based studies [32, 33] have shown in the last decade that the inclusion of information of local context (i.e. information about the surroundings of the target object) may improve model performance [34, 35]. This information can be included in a learning model by either enlarging the receptive field size (i.e. widening the field of view) [31, 35, 36] or by incorporating context-aware features that encode neighboring information into the target object [37] (i.e. a specific tree in our case).

To our understading, to date there has not been proposed a standardized RS-based approach to add context into AGB regression experiments. Furthermore, it has not been fully investigated how spatial patterns and shifts of tree traits across environmental gradients can reveal the influence of environmental and biotic effects on the individual tree structure. Such patterns, as long as can be surveyed and incorporated into a RS framework, are relevant to AGB research. Specifically, the question that still remains unanswered is how context-awareness can be fully integrated in a RS framework and leveraged to enhance AGB estimates at the individual tree level. Here, we therefore developed a fully integrated RS framework to provide context information into regression analyses, independently from ancillary data sources, or metrics obtained from artificially bounded inventory plots. To meet that end, we i) collected close-range PCD via UAV-LiDAR surveying in a coniferous forest, ii) retrieved contextual information based on the geographic spatial association of tree heights, iii) integrated context into different regression experiments, and iv) evaluated the effect of introducing context-awareness in tree-level AGB estimates, in a monospecific Norway spruce forest.

This study introduces contextual learning to improve AGB estimates at the individual tree level based on methods fully native to UAV-LiDAR data. We posit that incorporating information related to the local forest structure, by informing the regression models of the height distribution of neighboring trees, results in more accurate predictions of tree-level AGB. The findings and method evaluation show that the prediction enhancement caused by including context-awareness, is robust across different models and in two separate datasets. Remarkably, our approach does not rely on additional data sources beyond the UAV-LiDAR datasets, which may facilitate transferability to other forest types and regions.

2 | MATERIALS AND METHODS

2.1 | Study Area

The Seehornwald Davos research site (46° 48’ 55.2"N, 9° 51’ 21.3" E, 1640m a.s.l.) is located in a managed subalpine coniferous forest on the western flank of the Seehorn mountain, near Davos, in the Swiss Alps. The site is labeled as a class-1 forest ecosystem station of the Integrated Carbon Ecosystem Station (ICOS) network [38] where regular forest inventory measurements are collected following standardized protocols. The site is covered by spruce trees (*Picea abies (L.) Karst*., > 99.5 %) with an average height and age of 14m and 100 years, respectively, while some trees reach a height of 40m and an age of 300 years. The stand parameters at the research site include tree density: 639 ± 311 tree/ha; basal area: 27.6 ± 16 m^2/ha; mean crown area of dominant canopy: 13.2 m^2; and mean DBH: 17.7 cm.

The site has not been affected by infrastructure development during the 20th-21st centuries. Since 1930, grazing livestock in the forest was abandoned, and the site is sustainably managed according to the Swiss Forest Law (1876, revised until 2017) [39]. Maps dating back to 1845 reveal minimal changes within the Davos-Seehornwald forest site, while slight effects of local harvests are noticeable, particularly on steeper slopes of the easter flank, and forest regrowth at the timberline can also be observed [40]. Patchy vegetation (i.e. dwarf shrubs and mosses) covers around 30% of the forest floor (acidic ferralic podzols), which lies on a mixed silicious and dolomitic bedrock. The research site is part of national (LWF [41], TreeNet [42], SwissFluxNet [43]) and international research networks (ICOS [44], ICP Forests [45], eLTER [46]).

The considered study area spans over 33 ha (Figure 1, b), and the terrain conditions are representative of the Alps around the Landwasser valley, i.e. a varying steepness of 23 ± 14°. The site lies on the eastern flank of the valley, so most of the slopes face west-southwest, i.e. mean slope aspect is 230°.

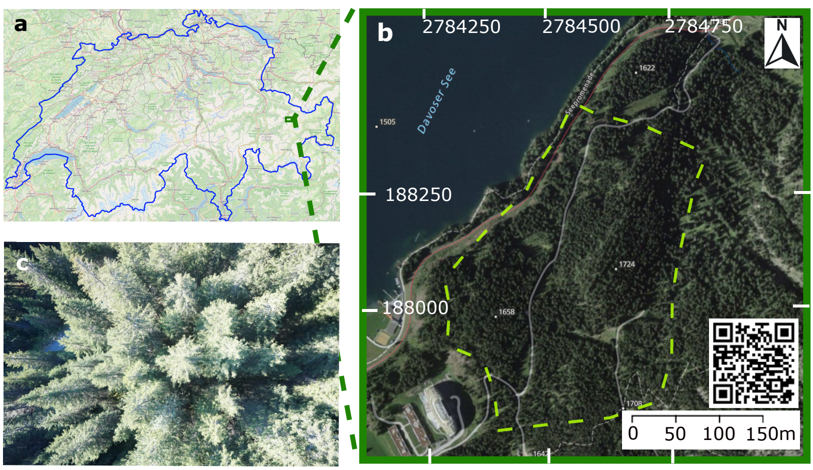

FIGURE 1 **a:** Location of the study site; the blue outline delineates the national territory of Switzerland (adapted from open.sourcemap.com). **b:** Orthoimage of the study site (adapted from swisstopo.admin.ch); coordinate units are in m, with LV95 as a projected reference system; the QR code links to additional information of the study site. The dashed yellow line shows the boundaries of the research site **c**: RGB image of forest canopy from a nadir angle taken during the survey.

2.2 | UAV-LiDAR Survey and Field-Based Measurements

We used a UAV-borne LiDAR system mounted to a DJI Matrice 600 Pro payload at a 90° pitch angle, and same heading and roll as the UAV platform. The system included a discrete infrared LiDAR scanner (M8 sensor, Quanenergy Systems, Inc. Sunyvale, CA, USA) and the corresponding state-of-the art inertial and navigation systems. In addition, we used a ground based Global Navigation Satellite System (GNSS, Trimble R8) during the UAV-LiDAR survey, set up in post-positioning kinematic (PPK) mode, which logged real-time satellite coverage (cf. Revenga et al. 2022 [47] for details on the airborne and ground system). The coupling of the satellite coverage data with the UAV-based laser and navigation data produced, allowed the generation of georeferenced point clouds, following Davidson et al. (2019) [48].

Data were acquired with a UAV flight height adapted to the terrain and tree height (Figure 2, a), ensuring a >20% overlap between individual LiDAR scans of ca. 50m width and 250 points/m^2. The surveys were conducted in October

2021, coinciding with the end of the forest growing season. Figure 2 (a) shows the trajectories of the individual UAV-LiDAR flights during the survey campaign. While the standard survey coverage followed a regular auto-pilot flight grid, certain flight lines had to be manually piloted to adapt to the topography and local forest structure. The digital elevation model of the study area is provided in Supporting Information (Annex V), to help to understand differences in flight heights.

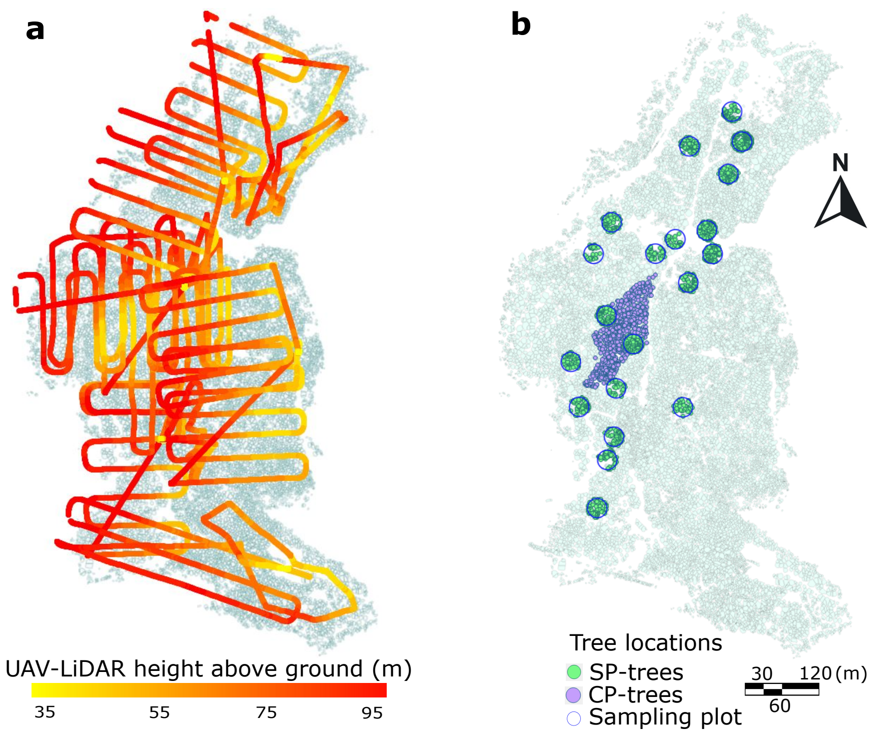

FIGURE 2 **a:** Trajectories of individual flights during survey of the Unstaffed Aerial Vehicle (UAV) Light Detection and Ranging (LiDAR) sensor; color gradient indicates height above ground during survey. **b:** Spatial distribution of field-based forest inventory. Dots represent the locations of the ground truth labels. The sampling plot-trees (SP-trees, N = 1635 trees) are shown in green; the control plot-trees (CP-trees, N = 845 trees) are shown in purple. In both **a** and **b**, the underlying polygon dataset shows the individual tree canopies (ITC) after the canopy height model (CHM) segmentation.

The field-based measurements (shown in Figure 2, b) are taken on a yearly basis as part of a long-term ecosystem monitoring initiative—jointly organized by ICOS [44] and the Swiss Federal Institute for Forest, Snow and Landscape Research (WSL) [41]. Based on standardized methods (i.e. *Sanasilva Inventory* protocol) [49], expert field workers monitor tree crown status, focusing on three groups of indicators: variations in size, density and color. The number of trees that have died since the previous survey, as well as the new ones that reached a minimum DBH of 5 cm are also recorded [50]. Tree height and DBH are monitored with a high-precision digital rangefinder (i.e. Vertex Laser Geo) and a standard calliper, respectively.

We treated two different datasets separately as ground truth measurements within the same study area: control plot trees (CP-trees, 4 adjacent monitoring units) and sampling plot trees (SP-trees, 20 scattered units of 15m radius).

The two datasets (i.e. SP- and CP-trees) are monitored by different research groups on the field and protocols presented minor differences between both datasets. Two main factors led us to consider both datasets separately: (i) the CP-dataset is clustered and spatially continuous, while the SP-dataset is spatially discontinuous and distributed along the study site (Figure 2, b); and (ii) the two datasets present some differences in morphological trait distribution (see Supporting Information, Annex IV). Figure 2 (b) shows the spatial distribution of the field-based forest inventory. The CP tree position was recorded using a Leica GPS1200 total station. The location and size of the sampling plots were defined according to ICOS protocols [51]. The center location of the SP plots was determined using a GNSS Leica CS20 (antenna GS15) with a real-time kinematic (RTK) signal (accuracy measurements ranges from 0.03m to 0.7m). Next, the trees in the SP plots were positioned by measuring the azimuth with a field goniometer, while the horizontal distance and the inclination from the plot centers was determined using a Vertex Laser Geo meter. The accuracy of foot location of trees in the SP plots is within 0.5m and 1.2 m. The field-based inventories used as ground truth contain measurements taken between October 2019 and July 2021. The changes in structural traits of max. two years between field-based measurements and UAV-LiDAR data aquisition were considered negligible for the purposes of this study (i.e. no disturbance events occurred).

2.3 | Method setup

The workflow followed in this study is presented in Figure 3. Initially, the PCD generation followed the approach described in Revenga et al. (2022) [47]. The resulting PCD scene was normalized and rasterized to obtain a canopy height model (CHM), which in turn was subject to individual tree crown segmentation [52] producing a two-dimensional polygon dataset. For the CHM segmentation, we utilized a watershed algorithm that is specifically designed for coniferous forests [52] (implemented in the LiDAR360 software [53]). The match between field-based measurements and individual tree crown (ITC) polygons was conducted based on the closest distance between the field-based GNSS point measurement and the ITC polygon centroid.

In order to ensure that only the LiDAR-detected trees would be accounted for in the regression experiment, a pre-processing manual task was undertaken (marked * in Figure 3). First, understory trees that passed unnoticed to the UAV-LiDAR survey were removed. Second, we filtered clumped trees based on tree height by selecting the field-based measurement of the highest tree when two measurements were less than 1m apart, while removing the measurement of the other tree. Third, we corrected for a crown shift effect, i.e. some high and skewed trees were affected by the presence of a smaller neighboring tree (affecting about 5% of trees) being closer to its corresponding ITC polygon centroid, thus introducing a wrong match between the field-based measurement and the LiDAR-derived metrics.

Afterwards, using the LiDAR-derived height as polygon attribute, we calculated the distance at which the spatial autocorrelation of tree height was most significant in order to define the optimal neighborhood size (as explained in Section 3.1). Once the optimal neighborhood size had been defined, we conducted the local indicators of spatial association (LISA) analysis [54, 55] and outlier analysis [56, 57] to retrieve neighborhood metrics. Finally, two separate supervised regression experiments were performed, in order to predict DBH based on LiDAR-derived metrics: one including the neighborhood metrics (context-aware regression), the other without taking those metrics into account (context-unaware regression). Finally, AGB was estimated from the predicted DBH via an allometric function (as defined in Eq. 5).

In parallel, we conducted a second task to characterize the morphometry of tree assemblages (i.e. groups of adjacent trees fulfilling a specific criterion of height similarity, as explained in Section 2.3) stemming from the ITC polygon dataset. Prior to the morphometric analysis of tree assemblages, a second pre-processing task was conducted (marked ** in Figure 3). First, ITC polygons were merged based on either local Moran's I_i [54] or SL_i [58] (see Section 2.3). These new larger polygons describe the two-dimensional projection of tree assemblages. Then, as our interest focused on the extent and shape of the tree assemblages, the inner borders of the merged polygons were disregarded. To reduce computation time, the polygon shapes were simplified by reducing the number of vertices and edges to 70 % while keeping the polygon shape.

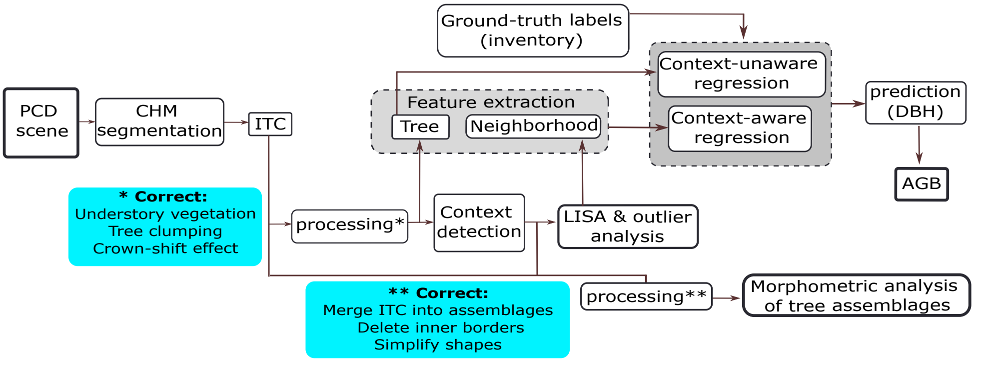

FIGURE 3 Workflow followed in this study. PCD: point cloud data, CHM: canopy height model, ITC: individual tree crown, LISA: local indicators of spatial association, DBH: diameter at breast-height, AGB: aboveground biomass. The two colored boxes describe the subtasks constituting each of the processing steps, marked * and ** in the diagram.

Definition of Context Via Tree Heights in the Neighborhood

We determined the distance at which neighborhood metrics should be calculated (i.e. how many surrounding trees should be accounted as neighbors) based on local similarity of tree height. Accordingly, the selection of an appropriate neighborhood size around each individual tree (i.e. context detection) [59] was calculated through the analysis of spatial autocorrelation of tree height as function of incremental distance, as in previous studies [60]. Based on the global peak in the significance of spatial autocorrelation, we defined a characteristic distance within which all included trees should be considered as neighbors. Then, all so-defined neighbor trees were accounted for to compute context-aware metrics.

The local context information was encoded as metrics derived from the distance-weighted individual tree heights in each neighborhood, calculated at each tree location. Specifically, the metrics computed to define the local context were: local Moran's I [54] (i.e. an estimate of local significance of tree height similarity with respect to the global variance); and (SL_i) of tree height (i.e. a weighted average of heights calculated entirely locally) [58].

Local Moran's I_i is a well-established distance statistic in spatial data analysis [61], used for detecting local spatial autocorrelation and included within the family of LISA methods [54, 55, 58]. Similarly to other geostatistics methods [62], it relates attribute similarity with locational similarity, mapping autocorrelation across the geographic space. In the following definitions, σ is the global sample standard deviation of tree height; n and m represent the total number of instances (i.e. all trees in the forest) and the number of neighbors to each tree, respectively; y_i indicates the magnitude of interest at a particular point of interest (i.e. tree height) while the overline (i.e.$\overline{y}$) indicates the global average; $w_{i,j}$ indicates the distance weighting of each neighboring tree (here defined as inverse distance weighting); subindexes i and j indicate the tree of interest and a neighbor tree, respectively. Let $y_1, \ldots, y_n$ be the tree height values of all the n trees in the dataset. Then, the Local Moran's I_i [54] is defined as

$$I_i = \frac{y_i - \overline{y}}{\sigma^2} \sum_{j \in \mathcal{N}_i, j \neq i} w_{i,j}(y_j - \overline{y}), \tag{1}$$

where $\mathcal{N}_i \subset \{1, \dots, n\}$ is the set of indices corresponding to the nearest neighbors of tree $i \in \{1, \dots, n\}$ in the overall set, where

$$\overline{y} = \frac{1}{n} \sum_{i=1}^{n} y_i, \tag{2}$$

and

$$\sigma = \sqrt{\frac{\sum_{i=1}^{n}(y_i - \overline{y})^2}{n-1}}, \tag{3}$$

are the global average height and the global sample standard deviation, respectively. It should be noted that insofar I_i includes global metrics (such as n, σ and $\overline{y}$), it is not entirely locally computed, but may present correlation with global features (i.e. characteristics derived from the entire dataset; cf. Westerholt et al. 2018) [63].

The Spatial Lag (SL_i) of tree height for a tree i is a spatial smoother [64] defined as:

$$SL_i = \sum_{j \in \mathcal{N}_i, j \neq i} w_{i,j} y_j \tag{4}$$

where the elements of the spatial weights matrix ($w_{i,j}$) are row-standardized, so that $\sum_{j \in \mathcal{N}_i, j \neq i} w_{i,j} = 1$. Therefore, SL_i can be seen as a weighted average of the heights of neighboring trees [65].

The neighborhood metrics finally chosen as context-aware predictors are the following: local Moran's Index (I_i), z-score of I_i, p-value of I_i, z-transformed value of I_i and SL_i—computed at 20 m, 30m , 40m and 50m distance bands. Additionally, the mean heights of the k-nearest trees, with k $\in (5 - 75)$, were also included as predictors. Likewise, we also included the topographic wetness index (TWI) [66] in order to evaluate the relative predictive performance of neighborhood metrics with respect to a well-established environmental variable as tree-growth predictor [67]. TWI is a steady state wetness index used to evaluate topography-dependent surface hydrology processes. According to the established definition [66], TWI is calculated as $\frac{a}{tan(b)}$, where a represents the upslope area draining through the point of interest, and b indicates the local slope. The parameterization considered to calculate TWI followed the suggestions of Kopecký et al. (2021) [68] for soil moisture estimation. In order to discern how much the contribution of TWI is influenced by granularity, we calculated it at a 2 m^2 resolution, and resampled to 5 and 10 m^2, via bilinear interpolation. Therefore, TWI was included at a spatial resolution of 2, 5 and 10 m^2 as separate predictors.

Finally, we included in the regression experiments predictive features informing of local neighbor dissimilarity, i.e. local outliers of tree height. We detected local outliers using Local Outlier Factor [56] and Isolation Forest [57] algorithms. The evaluation of these features allowed us to discern between the contribution of local similarity features (i.e. Local Moran's I_i and SL_i) and that of the local outliers.

Tree Assemblages' Morphometry

Utilizing the neighborhood metrics defined above, we computed tree assemblages within the study site. This enabled us to investigate whether the morphometry of such forest sectors would be useful as predictors of individual tree attributes (i.e. DBH, AGB). In order to define the tree assemblages, both local Moran's I_i and SL_i were computed at the optimal distance band to obtain neighborhood metrics, i.e. based on the global peak in the significance of spatial autocorrelation as a function of distance (using ArcGIS Pro) [69].

Tree assemblages were therefore defined as geographically continuous groups of trees delineated according to either (i) variation of local Moran's I_i of tree height, or (ii) according to quantiles of SL_i of tree height. The rationale for using two different statistics to calculate tree neighborhood metrics and thus delineate different tree assemblages was that while SL_i is entirely locally calculated, local Moran's I_i includes global features (and is therefore sensitive to the statistical characteristics of the dataset as a whole), as explained in Section 2.3. In order to discern which of the two approaches resulted most convenient in delineating tree assemblages (the former *entirely* local; the latter only *partially* local), both were included.

Tree assemblages defined according to local Moran's I_i are geographically continuous groups of trees with significantly different heights than the global tree height average, and they also lie in a region with significantly different neighbors. Local Moran's I_i identifies regions where the clustering of either high or short trees occurs. In the standard notation [58] (i.e. *High-High* or *Low-Low*), the first term refers to the individual tree and the second to the neighborhood (e.g. a tree belonging to a *High-High* assemblage is a "significantly high tree" in a "significantly high neighborhood"). The areas not showing statistical significance (thresholded at p-value $\geq$ 0.002) were labeled as *Not-Significant*. The significance test is based on random permutations (n = 499) of neighboring tree-height values at each step in the computation. The number of permutations and p-value indicate that, under the null hypothesis (i.e. tree heights being randomly distributed), a single tree canopy is likely to be wrongly classified with a probability of 0.002, which was deemed sufficient for the purpose of evaluating tree assemblage morphometry (i.e. if 1 out of 499 trees is wrongly attributed to a neighborhood, the morphometry of the neighborhood will not change significantly). Then, for every permutation, a local Moran's I_i value is calculated by randomly rearranging the tree heights of neighboring values. The result is a randomly generated reference distribution of expected local Moran's I_i that is compared against the observed local Moran's I_i (Eq. 1) [55]. In this way, tree assemblages defined according to local Moran's I_i are classified as: *High-High*, *Low-Low*, or *Not-Significant*.

Likewise, tree assemblages defined according to SL_i of tree height are geographically continuous groups of trees delimited according to the local weighted average of tree height [65], as defined above (Eq. 4). For the purpose of this study, 5 subdivisions based on quantiles were deemed convenient, rendering a classification of tree assemblages based on SL_i ranking as: *Highest*, *High*, *Mid*, *Low* and *Lowest*.

The morphometric analysis examined the outer boundaries of the tree assemblages, defined either by local Moran's I_i or SL_i of tree height, as defined above. Twenty basic morphometric parameters as well as 20 derived parameters were calculated for each type of tree assemblage. The 20 basic morphometric variables are simple parameters obtained by fitting elemental geometric shapes to each tree assemblage polygon (e.g. area of maximum inscribed circle), and basic positional parameters (e.g. XPOL, which is the X coordinate of the centroid of the tree assemblage polygon). The 20 derived parameters are adimensional metrics (except for concavity [70], measured in m) computed from the 20 basic morphometric variables, as explained in Güler et al. 2021, [71] (details are given in Supporting Information, Annex I). The morphometric analysis of tree assemblages was conducted using PolyMorph-2D algorithm [71], which is a toolbox for the morphometric analysis of vector-based polygon objects, available as a plug-in for the open source JumpGIS software [72].

Regression Models Selected

The regression experiments were designed to predict DBH, since AGB is a variable determined by the combination of DBH, height and wood density [9]. Instead, DBH is directly measured in the field, which makes it a better defined regression target. Therefore, the model estimates of AGB were derived from the DBH prediction outputs by means of an allometric fit (Eq. 5). Predicting DBH, instead of AGB directly was chosen as more suitable, as it avoids burdening the learning models with the statistical error contained in the allometric fit. Three feature-based regression methods were selected: namely AdaBoost [73, 74, 75], Lasso [76] and Random Forest [77] regressors. The AdaBoost regressor employs a gradient-boosting method that relies on stage-wise additive expansions. Its effectiveness stems from combining weak learners, i.e. decision trees, to form a generalized prediction hypothesis. Lasso, on the other hand, is a linear model with an *L1* prior penalty acting as a regularizer [78]. Random Forest is a well known tree-based ensemble regression method. In our case, all three regression methods utilize the features derived from the ITC polygon dataset resulting from the CHM segmentation.

Context-unaware regressions were defined as those in which a learning model performs DBH regression by taking as predictors only individual tree attributes derived from the ITC polygon dataset (i.e. tree height, canopy area and canopy perimeter), as it is a common approach [8]. On the other hand, we defined context-aware regressions as those regressions in which context-aware features are additionally introduced as input in the predicting feature space. These were either neighborhood metrics, e.g. SL_i of tree height, or TWI at different spatial resolutions (see Section 2.3) . For every model predicting DBH from individual tree attributes (i.e. context-unaware conditions) we implemented a context-aware counterpart. This allowed us to evaluate the impact of context on regression model performance.

Model Training and Validation of Results

A hard validation of AGB is not possible without harvesting trees destructively, which raises obvious ethical, legal and economic issues. Instead, non-invasive methods that use RS data and allometric functions are the standard procedure for estimating AGB [79]. Here, we estimated AGB from tree height, DBH, wood density and an allometric function (eq. 5). The regression analyses conducted are focused on comparing performance of predictions on DBH between models (i) "context-unaware" and their (ii) "context-aware" counterparts.

We chose DBH as the variable to test model predictions, which is a tree morphological trait contained in the field-based forest inventory, and therefore directly measured by *in situ* monitoring. Next, in order to assess the benefits of including context in the regression models, we compared results using AGB of individual trees. Hence, AGB estimates were derived via species-specific allometric and wood density functions, tree height retrieved via UAV-LiDAR, and DBH predicted via ML regression. Specifically, the allometric model used was the one proposed by Dalponte and Coomes (2016) [9]:

$$AGB_{tree} = \alpha \cdot WD^{\beta}_{spruce} \cdot (DBH - d_0)^{\gamma} \cdot H^{\delta}, \tag{5}$$

where the wood density value (WD_{spruce}) was taken from Alpine spruce dendrometric models [80], *DBH* was predicted via ML regression and height (*H*) was extracted from the UAV-LiDAR data. $\alpha, \beta, \gamma, \delta$ and d_0 are species-specific fitted allometric parameters [81], obtained from allomeric fits to harvested spruce trees by the Forestry and Wildlife Service Agency of the province of Trento (an Italian neighbouring province southeast from the study site, also used in Dalponte and Coomes, 2016) [9], and we consider them applicable to the Seehornwald Davos research site.

At all events, for the purpose of assessing the benefits of a context-aware approach, the specific characteristics of the allometric fit used are negligible, as it is only used to quantify a difference in terms of AGB, and both types of predictions (unaware and aware) take the same equation. Therefore, the predicted value of DBH (in either aware or unaware conditions) was input into Eq. 5, in order to obtain model predictions of AGB. This allowed to compare AGB predictions with the ground truth values of AGB, which were similarly obtained via the field-based measurements (provided by the regular tree-monitoring campaigns of ICOS [44] and WSL [41]) and Eq. 5.

For training and validating the regression models, the instances with empty ground truth labels were initially removed (i.e. trees with no DBH or tree height recorded). Afterwards, data stratification was performed via five commonly used percentiles (i.e. 0-10, 10-25, 25-50, 50-75, 75-90, 90-100) to ensure that the input data are independently drawn from an identical sample distribution (IID assumption) [82]. This assured us that most parts of the target distribution are represented, in particular the tail ends.

The technique used to estimate model prediction error consisted of a nested cross-validation (NCV) scheme [83]. Following the NCV scheme, we divided the input dataset into 10 inner and 10 outer folds. In NCV, the results in the inner folds report of the training performance, and they are used for model optimization, while the mean performance on the outer folds is the one used for model evaluation. The model inspection technique used to evaluate predictors' influence on the DBH regression results was the permutation importance method as proposed by Altmann et al. (2010) [84]. The feature-elimination procedure consisted of eliminating progressively those predictors that presented a negative mean importance, as they were considered harmful to the model's performance. The significance of the enhancement in context-aware predictions and effect size was assessed using Wilcoxon signed-rank test [85] and Cliff's Delta analysis [86], respectively.

3 | RESULTS

3.1 | Context Detection and Tree Assemblage

The analysis of spatial autocorrelation of tree height as function of incremental distance resulted in a maximum significance at a distance of 40 m. Figure 4 (a) shows the calculation of local Moran's index (I_i) of tree height at different distance bands. Figure 4 (b) shows the z-score of I_i obtained at each distance band, resulting from comparing the observed I_i and the expected I_i under the tree height randomness assumption (details included in the Annex II). As a precaution, we ran context-aware regression experiments including also context features retrieved at shorter (i.e. 20m, 30m) and larger (i.e. 50m) distances than the optimal range (i.e. 40m). The context features retrieved at these distances and that contributed to improved predictions of DBH (i.e. 20, 30, 40 50m) were all included in the final regression models.

In Figure 5, panels a and b show the spatial distribution of tree assemblages calculated using either local Moran's I_i or SL_i of tree height, respectively, at 40m range. While both types of assemblages show similarities as regards extent, morphometry and location, SL_i captures more local variability. This is not only due to a higher discretization (5 groups in SL_i, vs. 3 groups in local Moran's I_i), but also to the fact that SL_i is insensitive to the variance in the dataset beyond the range of its neighborhood, as explained in Section 2.3.

The morphometric analysis provided 40 additional features that were evaluated as potential predictors of DBH. In Figure 6, panels a and b visualize the results of the morphometry analysis of tree assemblages defined by local Moran's I_i and by SL_i, respectively. The circular barplots show the average magnitude as bar lengths, and the standard deviation as dots. Both mean and standard deviation values are shown as min-max scaled (across assemblage types) to present all variables on the same radial axis and to ease visual comparison, i.e. for every morphometric variable,

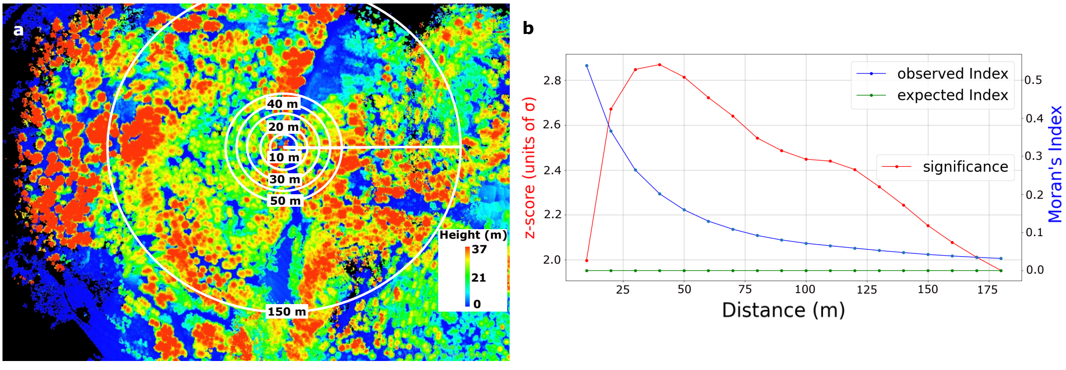

FIGURE 4 Context detection. **a:** Normalized point cloud data (PCD) scene colored by tree height overlaid with a selection of the appropriate radii for defining the neighboring context. **b:** Autocorrelation of tree height as function of distance. The red line shows the number of standard deviations (σ) that an observation is away from the expected value (under the assumption of heights being randomly distributed). The blue and green lines show the actually observed local Moran's Index and the expected value under randomness assumption, respectively.

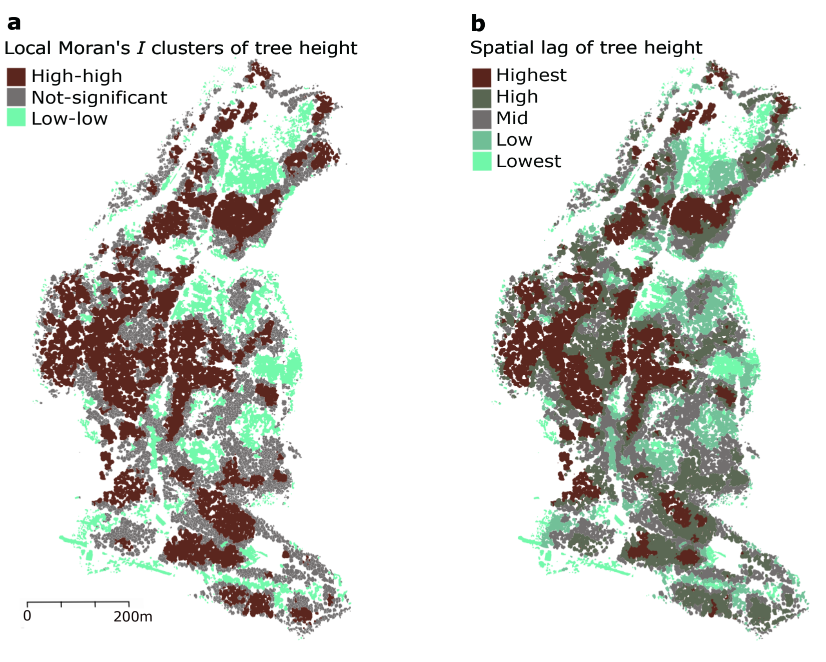

FIGURE 5 Tree assemblages defined by local similarity of tree height. **a:** Delineated according to local Moran's I_i of tree height. **b:** Delineated according to spatial lag of tree height.

the highest value is replaced by 1, the minimum is replaced by 0, and the intermediate values are linearly interpolated between 0-1.

It can be observed (Figure 6) that the morphometric variables follow very similar trends when tree assemblages

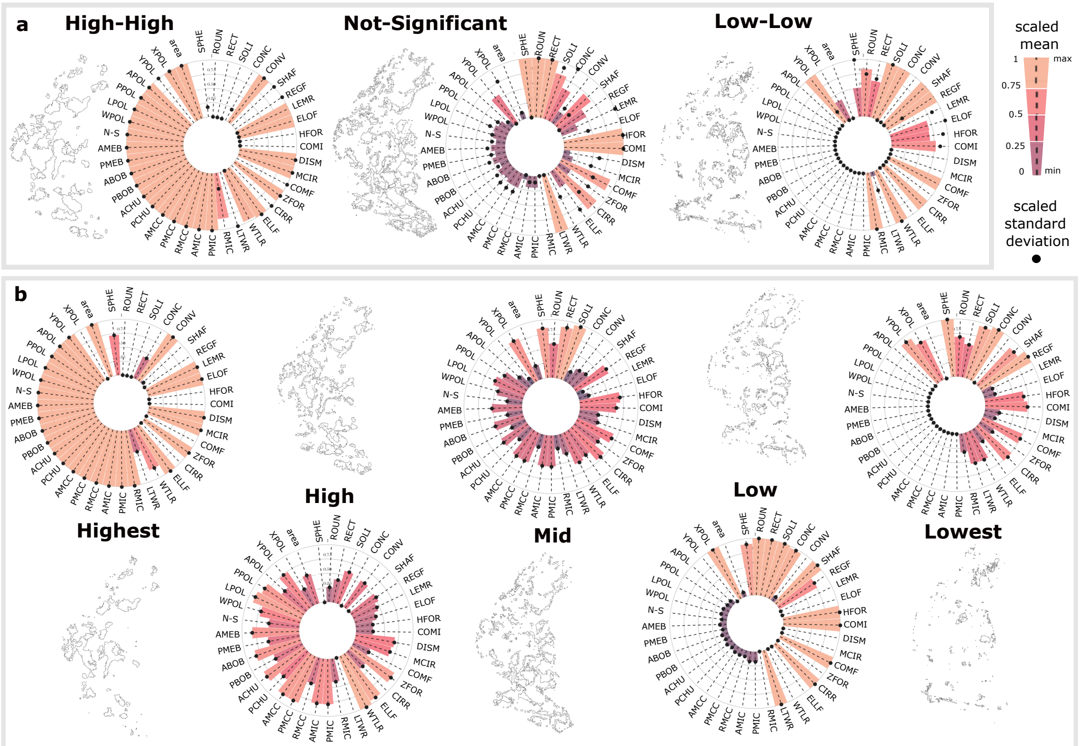

FIGURE 6 Morphometric analysis of tree assemblages grouped by **(a)** local Moran's I_i, and **(b)** by spatial lag of tree height. Bar length and color gradient represent the mean value, while black dots represent the standard deviation (SD) over all tree assemblages. Both mean and SD are scaled (min-max) to allow comparison of all metrics across assemblage types on the same axis—i.e. for every morphometric variable, the highest value of a certain assemblage type is replaced by 1, the minimum value is replaced by 0, and the intermediate values are linearly interpolated in between the range (0-1). YPOL: northing of centroid of the tree assemblage; XPOL: easting of centroid of the assemblage; APOL: area of polygon (P); N-S: defined as $|sin(azimuth)|$, shows the alignment of the main axis of P with the North-South direction; PPOL: perimeter of P; LPOL: major axis length (L) of P; WPOL: minor axis length (W) of P; ABOB: area of the bounding box fully containing P; PBOB: perimeter the bounding box fully containing P; AMEB: area of the minimum enclosing box fully containing P; PMEB: perimeter of the minimum enclosing box fully containing P; ACHU: area of containing hull ; PCHU: perimeter of convex hull fully containing P; AMCC: area of the minimum circumscribed circle (MCC); PMCC: perimeter of MCC; RMCC: radius of MCC; AMIC: area of maximum inscribed circle (MIC); PMIC: perimeter of MIC; perimeter of MCC; RMIC: radius of MCC; LTWR: length-to-width ratio [87]; WTLR: width-to-length ratio [88]; ELLF: ellipticity factor [89]; CIRR: circularity ratio [90]; ZFOR: Zavoianu's form factor [91]; COMF: compactness factor [71]; MCIR: Miller's circularity ratio [92]; DISM: dispersion measure [90]; COMI: complexity index [71]; HFOR: Horton's form factor [87];ELOF: elongation ratio [93]; LEMR: lemniscate ratio [94]; REGF: regularity factor [89]; SHAF: shape factor [89]; CONV: convexity [95]; CONC: concavity [70]; SOLI: solidity [96]; RECT: rectangularity [97]; ROUN: roundness [95]; SPHE: sphericity [98].

are defined based on local Moran's I_i or SL_i. However, an observed difference between SL_i and local Moran's I_i was found in the heteroscedasticity of the morphometric variables calculated. In the former case, we observed that the variance of all metrics scaled with magnitude (i.e. constantly increasing variance), while in the latter an irregular trend was found (i.e. an uneven trend in the variance). We visualized these observations in the distribution of scaled mean values and scaled standard deviations in Figure 6, a and b.

While not for all variables a systematic trend was found, for several basic morphometric variables a linear positive correlation between them and SL_i was observed, as shown by the calculated Pearson coefficient (ρ). This is the case for polygon area (ρ= 0.95), perimeter of polygon (PPOL; ρ=0.98) and radius of the minimum circumscribed circle (RMCC; ρ=0.98). Additionally, a positive correlation was found for some derived morphometric variables, namely: length-to-width ratio (LTWR; ρ=0.75) [87], circularity ratio (CIRR; ρ=0.88) [90], compactness factor (COMF; ρ=0.89) [71], dispersion measure (DISM; ρ=0.90) [90], complexity index (COMI; ρ=0.88) [71], lemniscate ratio (LEMR; ρ=0.81) [94], regularity factor (REGF; ρ=0.82) [89], and concavity (CONC; ρ=0.96) [70]. Conversely, other morphometric variables showed a decreasing trend with increasing SL_i. A clearly negative correlation between SL_i and the following derived morphometric variables was found: Miller's circularity ratio (MCIR; ρ=-0.88) [92], Horton's form factor (HFOR; ρ=-0.88) [87], elongation factor (ELOF; ρ=-0.83) [93], shape factor (SHAF; ρ=-0.95) [89], rectangularity (RECT; ρ=-0.85) [97] and roundness (ROUN; ρ=-0.69) [95].

3.2 | AGB Predictions: Aware vs. Unaware of Local Context

Regression experiments including context-aware features improved predictions of DBH consistently (see Tables 1 and 2), resulting in spatially resolved enhanced tree-level AGB predictions via allometry (Eq. 5). Although consistent, the degree of prediction enhancement differed between both datasets considered. Predictions in the CP-dataset observed a lower enhancement in comparison to predictions in the SP-dataset. For instance, RMSE was reduced by 9.1% (SP-dataset) vs. 4.0% (CP-dataset), and R^2 increased by 3.5% (SP-dataset) vs. 3.2% (CP-dataset). This was expected, due to less variability in context in the CP-dataset.

In Figure 7 (a) shows the ground truth labels (i.e. field based estimates of AGB), which were derived from the field measurements and a species-specific allometric fit (i.e. Eq. 5). The central panel (b) shows the spatial distribution of residuals (i.e. $\epsilon = AGB_{ground-truth} - AGB_{prediction}$) of the AdaBoost context-aware regression results. The mean values converge towards zero (i.e. $\bar{\epsilon}_{SP} = 3.8$ kg , $\bar{\epsilon}_{CP} = -3.2$ kg), while the spread of the error distribution varies between SP and CP-datasets (i.e. $\sigma(\epsilon_{SP}) = 123$ kg, $\sigma(\epsilon_{CP}) = 140$ kg).

In Figure 7 (b) we visualized the lack of high spatial autocorrelation of errors (i.e. low clustering of errors), indicating that predictions are not geographically biased. Figure 7, panel c, displays the error distributions in both datasets. SP-errors show a unimodal distribution with a slight overestimation of DBH of -28 mm. CP-errors present a similar overestimation bias (-25 mm) with a bimodal distribution (the second mode is located at 25 mm of underestimation). The second mode of the bimodal pattern in the CP-dataset may correspond to the more frequent occurrence of larger trees, which tend to be underestimated (Figure 7, c, lower panels). It can be observed that, generally, smaller and thinner trees tend to be slightly overestimated (i.e. in the first two quantiles) compared to the largest trees, which tend to be underestimated.

Figure 8 presents the analysis of the relative importance of all predictors considered in the context-aware DBH regression with the AdaBoost regression model (i.e. the best performing one). The analysis reveals that in both SP- and CP-datasets, the most important context-based predictors are the average heights of the 5, 10, and 15 nearest neighboring trees, outperforming some individual-tree metrics, such as the crown metrics.

TWI made a marginal contribution to enhanced predictions, which was less than that of any neighborhood metric. It exhibited a greater impact on improved predictive performance at finer spatial resolutions in both datasets (Figure 8), whereas its contribution decreased at coarser resolutions (e.g. it did not significantly contribute as a predictor at 10m resolution). This observation indicates that the spatial resolution at which TWI is most informative of individual tree traits, is similar to the usual tree crown size (i.e. 2-5m resolution), while at a coarser spatial resolution its contribution as predictor becomes negligible.

TABLE 1 Results (on test set) of the sampling plot (SP) dataset. Predictor variables are LiDAR-derived features; target variable is diameter at breast-height (DBH, in mm). The values are presented as mean ± standard deviation of the 10 outer CV folds of the nested scheme. One asterisk (*) marks results where the enhancement introduced by context-awareness is statistically significant with "small" size effect, while ** and *** mark "medium" and "large" size effect, respectively. The best results are shown in bold.

Regression model	R^2	RMSE (mm)	MAE (mm)	MAPE (%)
AdaBoost (unaware)	0.830 ± 0.05	58.0 ± 9.0	43.3 ± 4.4	19.1 ± 1.9
AdaBoost (aware)	**0.860** ± **0.03** ***	**52.7** ± **5.3** ***	**41.0** ± **3.1** **	**19.5** ± **1.7**
Random Forest (unaware)	0.818 ± 0.04	60.2 ± 7.3	46.8 ± 4.5	22.8 ± 5.8
Random Forest (aware)	0.838 ± 0.05 *	56.5 ± 9.2 *	41.6 ± 5.4 ***	22.4 ± 5.1
Lasso (unaware)	0.851 ± 0.02	54.6 ± 4.9	4.20 ± 3.3	19.1 ± 1.4
Lasso (aware)	0.852 ± 0.02	54.4 ± 4.9	4.17 ± 3.5	18.8 ± 1.7

TABLE 2 Results (on test set) of the control plot (CP) dataset. The predictive variables are LiDAR-derived features; the target variable is diameter at breast-height (DBH, in mm). The values are presented as mean ± standard deviation of the 10 outer CV folds of the nested scheme. One asterisk (*) marks results where the enhancement introduced by context-awareness is statistically significant with "small" size effect. The best results are shown in bold.

Regression model	R^2	RMSE (mm)	MAE (mm)	MAPE (%)
AdaBoost (unaware)	0.713 ± 0.07	54.7 ± 5.98	43.0 ± 5.26	15.5 ± 2.4
AdaBoost (aware)	0.737 ± 0.05 *	52.9 ± 5.28 *	42.2 ± 4.43 *	15.7 ± 3.1
Random Forest (unaware)	0.688 ± 0.07	57.0 ± 5.9	43.8± 5.1	15.7 ± 3.1
Random Forest (aware)	0.705 ± 0.04	55.6 ± 5.3	41.3 ± 5.5 *	15.9 ± 4.3
Lasso (unaware)	0.741 ± 0.09	51.3 ± 6.6	39.1 ± 5.2	13.6 ± 1.6
Lasso (aware)	**0.750** ± **0.08**	**50.4** ± **5.9**	**38.6** ± **4.1**	**13.6** ± **1.1**

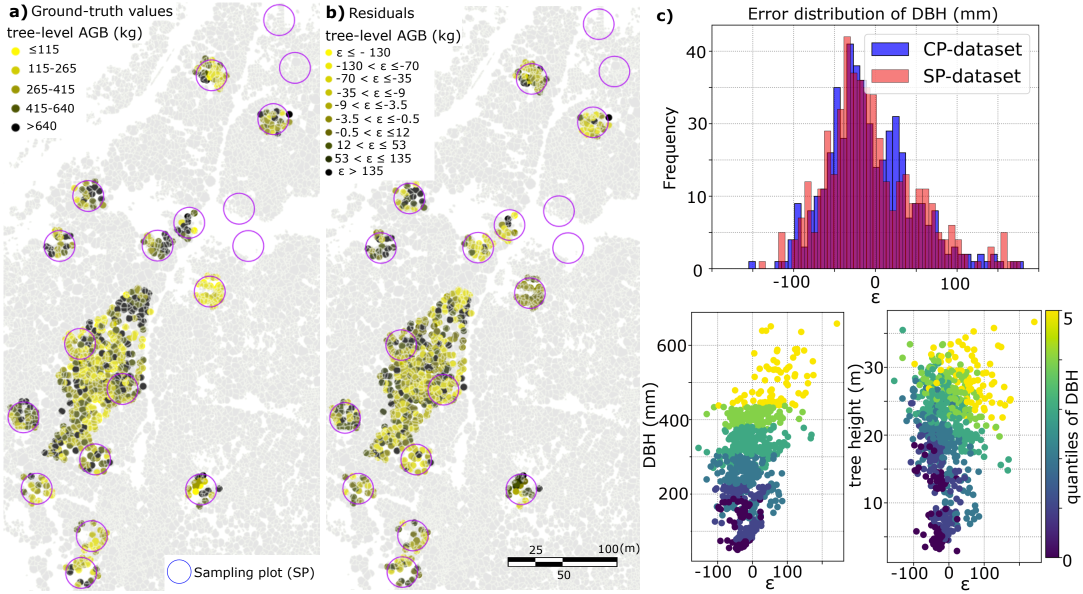

FIGURE 7 **a**: Spatial distribution of tree-level aboveground biomass (AGB) according to ground truth measurements (provided by the tree-monitoring campaigns of ICOS [44] and WSL [41]) and Eq. 5, grouped by quantiles. **b:** Spatial distribution of residuals ($\epsilon = AGB_{ground-truth} - AGB_{prediction}$) of AGB predictions with AdaBoost context-aware regression, grouped by quantiles. Negative values indicate overestimation. The four empty SP-plots (and the southernmost one not included) correspond to areas where the quality of the UAV-LiDAR data collection was compromised; in such five plots, due to high level of noise in the point cloud data, all data were rejected (see Supporing Information, Annex V). **c**: error distributions of diameter at breast-height (DBH) in sampling plot (SP) and control plot (CP) datasets. The two bottom-right panels show the error distribution of DBH (in x-axis) vs. field-measurements of DBH and tree height. Colors representing quantiles do not entirely show a sharp separation (especially below 200 mm of DBH) because the quantiles refer to each dataset separately, which are differently distributed, as it is shown in Annex IV. For clarity, we opted to present all available data together, encompassing both datasets.

434

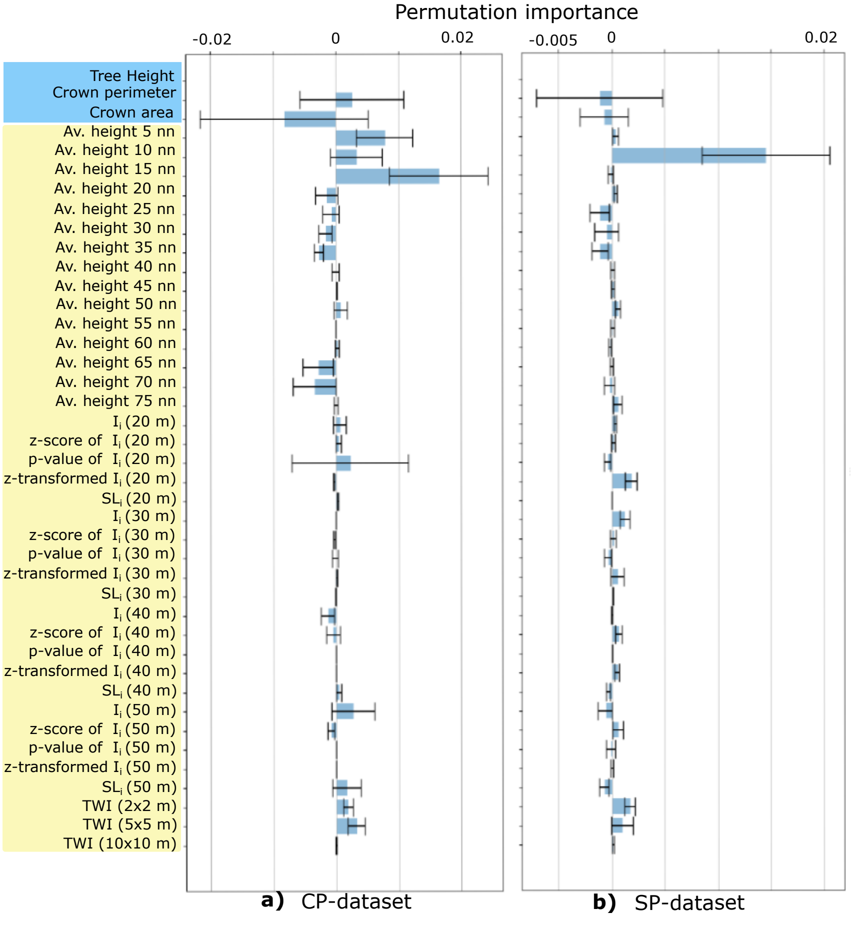

FIGURE 8 Inspection of predictors' importance via the permutation method [84] in AdaBoost regression experiment in context-aware conditions. The left panel **(a)** shows results in the control plot (CP)-dataset, and the right panel **(b)** shows results in the sampling plot (SP)-dataset. Bar length and error bar show the mean and standard deviation of a predictor's importance, respectively. A negative mean value indicates that a predictor is less useful than when being randomly shuffled, so it lowers the model's predicting performance. Predictors highlighted in light blue are individual tree traits; predictors highlighted in light yellow are context-based (i.e. either neighborhood metrics or TWI). In both datasets, it can be noted how the average heights of the nearest neighbors (nn) stand out as the strongest context-based predictors. In both plots (**a** and **b**), individual tree height (with importance: 0.85 in CP-trees; 1.3 in SP-trees) has been removed to ease visual comparison of the remaining predictors.

435

4 | DISCUSSION

4.1 | Enhancement of Tree-Level AGB Prediction

This study presents a method to enhance tree-level AGB estimates in coniferous forests using UAV-LiDAR surveying and context-aware ML regression methods, in line with established context learning literature [31, 32, 33, 34, 35, 36, 37], and forest research—e.g. NLME methods [13, 14, 15] and competition-based studies [16, 17, 18]. We further extend this approach to a fully integrated UAV-LiDAR framework. The results consistently showed that context-aware regressions outperformed context-unaware regressions across models (except for Lasso in the SP-dataset, where performance stagnated). This finding indicates that gradients in morphological tree traits across the ecosystem may be a proxy for hidden environmental and biotic mechanisms (e.g. windstorm disturbance, nutrient and soil moisture abundance, light harvesting competition) [99, 100] that influence tree growth, and can be leveraged to enhance predictions of AGB at the single tree level.

The accuracy enhancement gained from including context-aware features in the regression experiments varied between the two datasets considered (i.e. SP-trees and CP-trees). Context-aware regressions of DBH in SP-trees experienced greater enhancement than in CP-trees. This is consistent with the fact that the CP-dataset contains less variability of context, since it is a clustered and more homogeneous dataset, while the SP-dataset includes more variability in context-aware features (Figure 2, b). The investigated spruce forest presents a heterogeneous landscape, where the distribution of tree heights varies in space. Hence, the UAV-LiDAR survey gives rise to a non-stationary tree dataset [59], showing both smooth gradients and sharp changes in height values, a non-trivial question in tree-phenotyping and functional trait mapping [31]. As SP-trees are grouped in scattered plots across the forest, their spatial distribution spans hundreds of meters, making them subject to a more diverse context than the very local CP-dataset.

4.2 | The Role of Neighboring Context in AGB Prediction Performance

Most regression models achieved enhanced predictions when contextual information was included, with results consistently showing no deterioration. Thereby, the degree of local similarity of tree height (i.e. SL_i, local Moran's I_i) was most important and, to a lesser extent, the LiDAR-based TWI, indicating that although TWI is a good predictor of tree growth [67], the neighborhood information resulted more significant, in agreement with previous literature [20]. Conversely, including features informing about neighbor dissimilarity, such as local outliers of tree height detected using Local Outlier Factor [56] and Isolation Forest [57] algorithms did not result in enhanced predictions. We hypothesize that metrics containing information about the degree of local similarity may reveal the combined effect of ecological processes that are specific to the immediate neighboring context. Conversely, metrics containing information of the dissimilarities of the individual trees do not help to uncover such processes, although they remain useful in detecting outstanding trees (i.e. local outliers).

Context-based features at closer distances generally showed larger predictive power but also larger variance (as less neighboring trees are computed), therefore producing a strong and fluctuating signal, that in some cases was challenging for the ML model to incorporate in the learning process. For instance, the p-value of Local Moran's I_i at a 20m range in the CP-dataset has an average positive effect but is not a stable predictor (Figure 8, a). This can be observed in the general trend of larger standard deviations in the permutation importance of predictors retrieved at short ranges than at greater distances (Figure 8). After the peak in the spatial autocorrelation of tree height (i.e. at larger distance bands than 40m) , the significance of clustering of tree height values declined, presenting another shoulder at a distance of 110m (Figure 4, b). As the neighborhood size increased beyond the 40-meter distance range, the predictive power of the metrics derived from the neighboring trees (i.e. the influence of local context) progressively smoothened down [64].

In accordance with competition-based studies [16, 17, 18], we observe that the strongest context-based predictors are those retrieved from the immediate neighboring trees in both datasets, i.e. the average height of 5, 10 and 15 nearest neighbors (Figure 8). However, our method additionally allows to compare the relative importance of competition-derived metrics and other context-based metrics operating at larger scales. For instance, in Figure 8 (a) it is shown that local Moran's I_i retrieved at a 50 m range is comparable in importance to the average height of the closest 10 neighboring trees.

A general difference observed between the CP and the SP-datasets is that the predictors' importances in the CP-dataset fluctuate more (i.e. larger standard deviations). Further, in the SP-dataset, predictors rarely become negative and if they do, it is to a lesser extent. Given its broader spatial distribution and greater contextual variability, we contend that the SP-dataset can be regarded as a more representative sample of the entire forest population compared to the clustered CP-dataset. Consequently, the finding that context-based features demonstrate greater stability within the SP-dataset is noteworthy.

Including morphometric variables calculated from the tree assemblages in the regression experiments—either defined by SL_i or by local Moran's I_i—did not result in improved predictions of DBH. The analysis of shapes of the tree assemblages revealed a convergence assembly pattern of tree heights [101], which was specially remarkable in certain metrics (e.g. concavity [70] and length-to-width ratio [87]), as discussed in Section 4.3. Nevertheless, none of the morphometric variables obtained from the tree assemblage analysis proved useful to improve predictions of DBH.

Considering context metrics to enhance estimates of DBH at the individual tree level has previously been suggested in seminal works [22, 102] and been adopted subsequently for various applications in forest research [21, 23]. Lo and Lin (2012) [18] proposed a competition-specific index to capture the effect of the competing pressure of immediate neighbors. Recent investigations on tree morphology and productivity [16, 17] have motivated the further development of competition-aware approaches to improve the prediction accuracy of individual tree traits, using overstory tree traits as predictors, such as tree height and crown metrics, which encourages the potential transferability of these methods to a fully integrated RS framework.

In forest biomass research, a commonly recognized approach is calibrating regression models with plot-level metrics for predicting tree-level structural traits (e.g. parameters accounting for plot-level random effects in NLME methods), which has been pointed out as a methodological limitation [20]. Indeed, the results of such approaches are constrained by the artificially-delineated plot size, and it has been observed that accuracy increases with plot size and number of tree neighbors [13, 15]. Furthermore, how diverse context-based attributes retrieved at different distance ranges affect tree-level predictions had not been investigated before. In this regard, our results show that the variability and extent of context determines its beneficial leverage for prediction of tree-level traits (e.g. DBH, AGB).

Our study continues this line of work and sheds light on how the local spatial context can be defined and leveraged in tree-level structural trait predictions (i.e. DBH), making a case for AGB estimates. The analysis shows that there is an optimal range to computing neighborhood metrics. In the case of the spruce forest studied here, this corresponded to a 40 m range distance, based on the spatial autocorrelation of tree heights. Further, we found that the predictive power of context-based metrics is sensitive to context extent (i.e. the range at which such metrics are calculated). This observation indicates that considering context based on plot-level metrics retrieved from artificially bounded units (plot-level metrics, as in [13, 14, 15]) may be seen as a constrained approach, as observed previously [20, 103]. Likewise, in the light of this observation, and in line with recent studies [104], determining the significant contextual extent of individual functional traits based on units of fixed size (e.g. pixel size) appears to be a suboptimal technique. Therefore, future forest research would probably benefit from including context-awareness determined by spatial association of tree traits, bearing in mind that context-detection is trait-dependent and may vary depending on dataset source—e.g. spatial autocorrelation as a function of distance (Figure 4) is sensitive to CHM segmentation quality—and method applied—e.g. delineation of tree assemblages varied slightly between local Moran's I_i, and SL_i, as we show in Figure 5. The motivation for our study has been to introduce more quantifiable terms to ecological reasoning and to propose a standardized method of incorporating context-awareness into AGB research. The method proposed is conceived for a fully integrated RS framework. Since we do not make use of external data sources but, on the contrary, every predictor is native to the UAV-LiDAR dataset, and we do not use understory vegetation metrics, the method may be easily transferable.

Lastly, we note that RS studies usually define the optimal scale of analysis as a trade-off between the observational extent (i.e. area surveyed) and the unit resolution (i.e. pixel size) [104]. Also, in ecological research, it is common to subsample datasets using natural subregions based on ancillary ecological criteria (e.g. ecoregions, conservation status) [105]. Conversely, here we defined the range of influence of context-based metrics (i.e. the extent of tree neighborhoods) using a dataset-native approach, based entirely on the spatial association of individual tree heights. This permitted us to determine the context of influence unhampered by the RS technique and not using external data sources. In computer vision studies that investigate contextual learning, image analyses typically do not assume a specific optimal scale [106, 107], such as in geographic analysis [108]. In this study, local context was defined based on the spatial association of a real physical attribute of the target objects (i.e. tree heights), and not defined by an artificially bounded unit (e.g. pixel size [109] or plot size) so that the resulting distance can be considered characteristic of the forest ecosystem.

4.3 | Tree Assemblages

The quantitative comparison of morphometric variables between tree assemblages (Figure 6) permitted to examine whether trees—grouped by local association of an individual trait—persistently show different shapes at the group level, shedding light on the relationship between context-based traits (e.g. concavity) and an individual tree trait (i.e. LiDAR-derived tree height). Remarkably, it was observed that tree assemblages delineated according to the weighted average of individual tree heights (i.e. SL_i) presented clear positive correlations with two-dimentional morphometric features at the group level.

For instance, assemblages with higher trees (i.e. labeled as *Highest* according to SL_i, or *High-High* according to local Moran's I_i) are consistently rounder, larger and more regular in shape. As visualized in Figure 6, SL_i correlates positively with shape regularity [89], two-dimensional concavity [70], length-to-width ratio [87] and size, indicating a consistent trait-convergence assembly pattern [101]. Higher trees seem to converge in most sheltered areas (i.e. thalwegs and local sub-basins) so that tree assemblages with highest SL_i tend to adopt the morphological features of the drainage network's shape (see Figure 9, in Annex I). Interpretation of this observation would go beyond the scope of this study. However, it may indicate that both the shape and location of tree assemblages of different heights are conditioned by underlying environmental and biotic driving mechanisms.

In the coniferous forest studied here, a significant degree of clustering of tree heights takes place (Figure 5, a), while spatial gradients of tree height present preferential shapes and directions (Figure 5, b). These observations indicate that there is tree-height convergence and a tendency toward optimal phenotype expression (i.e. maximum growth performance) around the runoff drainage network (Figure 9, c, in Annex I). Higher trees are found in sheltered regions and concave channels—which generally benefit from more frequent runoff events and deeper soils [110, 111].

This may indicate that favorable environmental conditions (e.g. deeper soil, lower soil moisture recession rates, greater availability of soil nutrients due to leaching) allow individuals to reach their optimal phenotype. Conversely, a lower SL_i of tree height in more exposed terrain (e.g. ridges, hilltops) indicates that environmental filtering (e.g. windstorm disturbance) or a reduced competition in light harvesting could play a significant role in determining the location of low SL_i tree assemblages (Figure 9, a, in Annex I). Thus, the relatively reduced tree height in exposed areas could indicate a passive response of tree height to harsher environmental conditions [112], an active response to higher light availability [99] or a limitation to tree growth caused by other local factors, such as lower soil depth or nutrients availability [1, 111]. Nevertheless, this study cannot provide an interpretation of such observations, as shifts in the variance of functional traits across environmental gradients (i.e. spatial patterns of trait similarity) do not bring strong evidence of either biotic or environmental filtering on their own [113].

4.4 | Methods Applied

We have aimed at preserving a fully-native LiDAR approach, so that the transferability of the method proposed is not compromised by lacking local ancillary data or other external data sources, which may become a limiting factor in forest monitoring. However, one main methodological constraint we acknowledge is that the strength of our results is currently limited by the lack of replicates at different forest sites. We cannot confidently confirm these findings to be generally applicable to a wider range of forest types beyond coniferous forests. Nevertheless, the enhancement in predictions was observed across most models and in two separate datasets. In sum, further research would be needed to evaluate the transferability of the method and contrast these findings across various tree species and stand configurations.

5 | CONCLUSIONS

This study is the first to introduce and evaluate a fully integrated UAV-LiDAR method that utilizes context information to improve the accuracy of AGB estimates of individual trees, making a case for a coniferous forest. The performance of the regression models consistently demonstrated improvements in AGB prediction when incorporating context-aware features. The exception was the Lasso model, which stagnated in the SP-dataset. Importantly, in no case did contextual features have a detrimental effect. We conclude from our results that the use of context-aware features as predicting variables can substantially improve estimates of AGB in coniferous forests—i.e. the best performing model showed a reduction of RMSE of 9.1 % and 4.0 %, and an increase in R^2 by 3.5 % and 3.2 %, in the SP- and CP-datasets, respectively. The different degree of enhancement in model performance between the two datasets is considered to be related to the contrasting variability in context between the CP-dataset (clustered and continuous) and the SP-dataset (discontinuous and scattered in twenty different plots across the study site). Features that provide information about the tree neighborhood (e.g. SL_i of tree height, average height of k-nearest trees) contain useful information to improve predictions of different individual tree traits (e.g. DBH, AGB). This finding suggests that the information retrieved from the local context serves as a proxy for underlying ecological mechanisms that exert influence on the individual tree AGB as a result of local adaptations to environmental and biotic processes.

We conclude that the proposed fully native UAV-LiDAR approach, which integrates spatial associations of tree heights, is more efficient in incorporating context compared to methods constrained by the use of data collected in artificially delineated monitoring plots. This is because at larger scales beyond the plot level, contextual features might play a role in improving AGB predictions. Moreover, as the method proposed uses metrics entirely native to the UAV-LiDAR dataset, it does not rely on tailored process-specific indices (e.g. competition metrics) or ancillary data sources (e.g. biome type, conservation status, ecoregions), making it potentially transferable to other regions and scales.

Author contributions

Original conceptual framework: JCR and SO; experimental design: JCR; UAV–LiDAR data collection: JCR; field-based data provision and curation: FS and MG; laser data pre- and postprocessing: JCR; feature engineering, training and evaluation of the machine learning models: JCR and SO; visualisation: JCR; supervision: AD, KT and FG; project administration: AD, NB, KT, FG and JCR; writing—original draft preparation: JCR; writing—review and editing: SO, MG, FS, FG, KT, NB, AD and JCR.

All authors have read and agreed to the published version of the manuscript.

Acknowledgements

Helpful discussions with Thomas Friborg, Daniel Kükenbrink and Moritz Bruggisser are gratefully acknowledged. Likewise, we acknowledge the contribution of the field workers, who are responsible for collecting the forest inventory data on a regular basis, used here as ground truth.

Funding

This project received funding support from the Talent Program Horizon 2020/Marie Skłodowska-Curie Actions, a Villum Experiment grant by the Velux Foundations, DK (MapCland project, number: 00028314), and the DeepCrop project (UCPH Strategic plan 2023 Data + Pool). MG also acknowledges funding by Swiss National Science Foundation project ICOS-CH Phase 3 (20F120_1982287).

Data avilability

The code, data and metadata that support the findings of this study are available from the corresponding author, JCR, upon responsible request, and will be published in a DOI-compliant public repository upon acceptance of this manuscript.

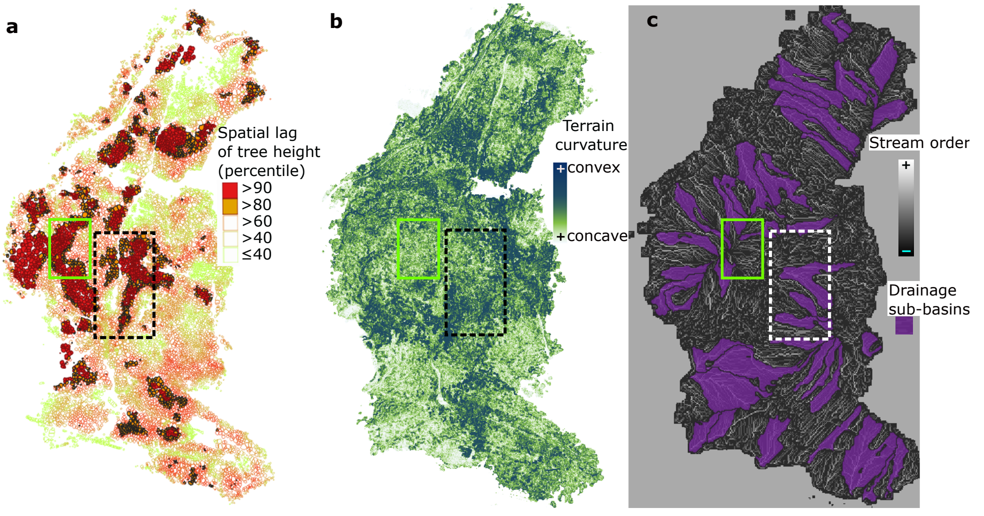

FIGURE 9 **a**: Spatial lag of tree height derived from the individual tree crown (ITC) polygon dataset. **b**: Map of terrain curvature derived from point cloud data (PCD) ground-returns. **c**: Hydrological network (Strahler's stream order) [114]. In all three panels, the dashed box indicates an area favored by surface hydrological conditions, hosting an assemblage of trees in the >90 % percentile of spatial lag of tree height. The solid green box indicates an area at a hilltop, unfavored by surface hydrological processes, more exposed to windstorm disturbance, and hosting an assemblage of trees in the < 60% percentile of spatial lag of tree height.

Supporting Information

| Annex I: Location and Morphometry of Tree Assemblages

The spatial distribution of SL_i presents directional anisotropy, stretching across preferential areas which seem to match sheltered sectors of the forest, such as concave thalwegs. Figure 9 highlights two neighboring areas with contrasting values of SL_i, indicating that surface hydrology processes and terrain exposure (i.e. terrain convexity) condition tree growth at the group level.

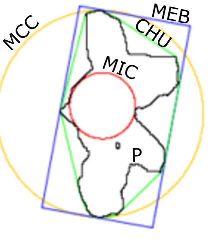

FIGURE 10 Calculation of elementary geometries fitted to an exemplary tree assemblage. P: polygon of tree assemblage (black line). MCC: minimum circumscribed cirle (in green). MIC: maximum inscribed circle (in red). CHU: convex hull (in yellow). MEB: minimum enclosing box containing P (in blue).

The morphometric analysis was conducted by taking into account the outer borders of tree assemblages defined either by SL_i, or by local Moran's I_i (delineated as explained in Section 2.3; results shownin Figure 5). The 20 basic morphometric variables (Table 3) result from fitting elementary geometries to the tree assemblage polygon. The 20 derived variables (Table 4) are adimensional parameters (except for concavity, in m^2) obtained by combining the basic parameters.

TABLE 3 Twenty basic morphometric variables derived from the tree assemblage polygon dataset (as described in Güler et al., 2021) [71]. P: polygon of a tree assemblage.

Basic parameters	Description	units
XPOL	Easting of P centroid	m
YPOL	Northing of P centroid	m
APOL	Area of P	m^2
PPOL	Perimeter of P	m
LPOL	Major axis' length of P	m
WPOL	Minor axis' length of P	m
N-S	North-South alignment of P, defined as $\lvert sin(azimuth) \rvert$ of major axis	$\varnothing$
ABOB	Area of the bounding box fully containing P	m^2
PBOB	Perimeter of the bounding box fully containing P	m
AMEB	Area of minimum enclosing box	m^2
PMEB	Perimeter of minimum enclosing box	m
ACHU	Area of the convex hull fully containing P	m^2
PCHU	Perimeter of the convex hull fully containing P	m
AMCC	Area of the minimum circumscribed circle enclosing P	m^2
PMCC	Perimeter of the minimum circumscribed circle enclosing P	m
RMCC	Radius of the minimum circumscribed circle enclosing P	m
AMIC	Area of the maximum inscribed circle enclosing P	m^2
PMIC	Perimeter of the maximum inscribed circle enclosing P	m
RMIC	Radius of the maximum inscribed circle enclosing P	m

TABLE 4 20 morphometric variables derived from the tree assemblage polygon dataset (as described in [71]). P: tree assemblage polygon. A: area of P. L: length of major axis of P. W: width of minor axis of P (i.e. width). ACHU: area of convex hull fully containing P. RMCC: radius of minimum circumscribed circle. PCHU: perimeter of convex hull fully containing P. AMEB: area of minimum enclosing box.

Derived parameters	Name	Definition	Source
LTWR	Length-to-width ratio	L/W	[87]
WTLR	Width-to-Length ratio	W/L	[88]
ELLF	Ellipticity Factor	$\lvert L-W\rvert/(L+W)$	[89]
CIRR	Circularity Ratio	P^2/A	[90]
ZFOR	Zăvoianu's Form Factor	$(16A)/P^2$	[91]
COMF	Compactness Factor	$P/(4\pi A)^{0.5}$	[71]
MCIR	Miller's Circularity Ratio	$(4\pi A)/P^2$	[92]
DISM	Dispersion Measure	$1-[(4\pi A)^{0.5}/P]$	[90]
COMI	Complexity Index	$1-[(4\pi A)/P^2]$	[71]
HFOR	Horton's Form Factor	A/L^2	[87]
ELOF	Elongation Factor	$(4A/\pi)^{0.5}/L$	[93]
LEMR	Lemniscate Ratio	$(\pi L^2)/4A$	[94]
REGF	Regularity Factor	$(\pi LW)/4A$	[89]
SHAF	Shape Factor	$[(4\pi A)/P^2]\times(L/W)$	[89]
CONV	Convexity	$PCHU/P$	[95]
CONC	Concavity	$ACHU-A$	[70]
SOLI	Solidity	$A/ACHU$	[96]
RECT	Rectangularity	$A/AMEB$	[97]
ROUN	Roundness	$(4\pi A)/(PCHU)^2$	[95]
SPHE	Sphericity	$(4A/\pi)^{0.5}/(2\times RMCC)$	[98]

Annex II: Context Detection

The distance range selected around each tree to compute neighborhood metrics (i.e. context detection), was conducted based on the peak of significance (determined using the standard z-score) of local spatial autocorrelation (using Local Moran's I_i) as function of increasing distance, in steps of 10 m.

Local Moran's I_i is a spatial statistic that relates attribute similarity to locational similarity, mapping the autocorrelation of individual tree heights across the geographical space, as defined above (Eq. 1, in Section 3.1). The expression below (Eq. 6) defines the z-score, which is used to measure the significance of tree-height clustering. Z-scores shows the significance of the clustering by subtracting the observed I_i values from the expectation (i.e. $E[I_i]$), and normalizing over the standard deviation of I_i. This produces a distance metric in units of standard deviations. $E[I_i]$ is the expected value of local Moran's I_i under the null hypothesis of no spatial autocorrelation.

$$z_{score} = \frac{I_i - E[I_i]}{\sqrt{V[I_i]}}, \tag{6}$$

Neighborhood size was determined according to the significance of spatial autocorrelation (defined as local Moran's I_i) as function of distance, via the standard z-score. Z-score measures the distance of a measured value from the expectation in units of standard deviation, under the assumption of randomly distributed values.

and the expected value of Moran's *I* under the null hypothesis of no spatial autocorrelation is:

$$E[I_i] = -\frac{\sum_{j=1}^{m} w_{i,j}}{m-1} = -\frac{1}{m-1}, \tag{7}$$

where *m* equals the total number of trees in the neighborhood. At large sample sizes (i.e. for increasing values of *m*), the expected value approaches zero. The spatial weights allocated to each neighboring tree *j* are standardized [65], such that for each tree *i*, $\sum_j w_{i,j} = 1$. The variance of local Moran's I_i is defined as the expectation of the square of I_i, minus the square of the expectations of I_i:

$$V[I_i] = E[I^2] - E[I_i]^2, \tag{8}$$

Annex III: Training, Validation and Test of results

Nested cross-validation (NCV) [83] follows the updated and established recommendations to achieve an unbiased estimate of the generalization error, while making optimal use of the limited available data. It is an evaluation method for determining the accuracy of point estimates and confidence intervals for prediction errors. As a modification developed from standard cross-validation [115], NCV improves estimates of prediction accuracy and confidence intervals by accounting for the correlation between error estimates in different folds, an inconvenient phenomenon affecting standard cross-validation that may render error estimates overly optimistic. How NCV is implemented is shown in Figure 11. The entire algorithmic routine of NCV is presented immediately below. The input data (i.e. *X*,*Y*) corresponds to the set of predictors (i.e. *X*), and the target variable DBH (i.e. *Y*), respectively.

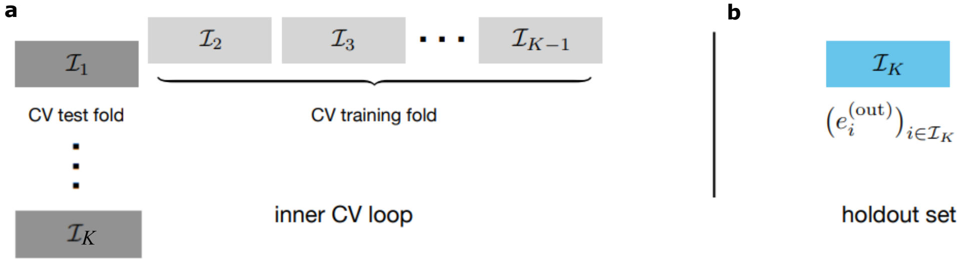

FIGURE 11 Visualization of 10-fold nested cross-validation (CV). **a**: at each of the *K* steps ($K = 10$), we perform standard cross-validation for model training (light grey folds), holding one of the folds out of the inner CV loop (dark grey fold). **b**: The fresh holdout folds (in blue) are never used for hyperparameter optimization or feature selection (figure adapted from Bates et al., 2021 [83]).

Algorithm 1: Nested cross-validation

Input: data (X, Y), fitting algorithm A, loss function l, number of folds K, number of repetitions R

```
procedure Nested cross-validation (X,Y)                    // ▷ primary algorithm;
    es ← []                                     // ▷ initialize empty vectors;
    a_list ← []                                 // ▷ (a) terms;
    b_list ← []                                 // ▷ (b) terms;
    for r ∈ {1, ..., R} do
        Randomly assign points to folds I_1, ..., I_K;
        for k ∈ {1, ..., K} do
                                                // ▷ outer CV loop ;
            e^(in) ← inner cross-validation(X, Y, {I_1, ..., I_K} \ I_k)      // ▷ inner CV loop ;
            θ̂ ← A((X_i, Y_i)_{i∈I\I_k}) ;
            e^(out) ← (l(f̂(X_i, θ̂), Y_i))_{i∈I_k} ;
            b_list ← append(a_list, (mean(e^(in)) − mean(e^(out)))^2) ;
            b_list ← append(b_list, var(e^(out))/|I_k|) ;
            es ← append(es, e^(in))
        MSE^ ← mean(a_list) − mean(b_list) ;
        Err^(NCV) ← mean(es) ;
        return: (Err^(NCV), MSE^)      // ▷ prediction error estimate and MSE estimate ;

procedure Inner cross-validation (X, Y, {I_1, ..., I_{K−1}})     // ▷ inner cross-validation subroutine ;
    e^(in) ← [] ;
    for k ∈ {1, ..., K − 1} do
        θ̂ ← A((X_i, Y_i)_{i∈I_i∪...∪I_{K−1\k}}) ;
        e^(temp) ← (l(f̂(X_i, θ̂)), Y_i))_{i∈I_k} ;
        e^(in) ← append(e^(in), e^(temp))
    return: e^(in) ;
```

Output: Nested cross-validation *(X,Y)*

Annex IV: Distribution Shift Between CP-trees and SP-trees

By morphological tree traits, we refer to the structural tree parameters considered in the study (i.e. tree height and DBH). Here below, we visualize the joint distributions of DBH and tree height in the two datasets considered in order to highlight how differently distributed they are.

The joint distributions of morphological tree traits DBH and tree height in both CP and SP-datasets show a shift between the two [82]. For instance, the kernel probability distribution of heights shows that the SP-dataset contains a higher amount of short trees (i.e. heights $\in (3, \ldots, 8)$ m), that cover a wide range of DBH values. Also, the range of DBH is broader in the SP-dataset compared to the CP-dataset, and the instances do not exhibit an accumulation in the center as evident as the one observed in the CP-dataset.

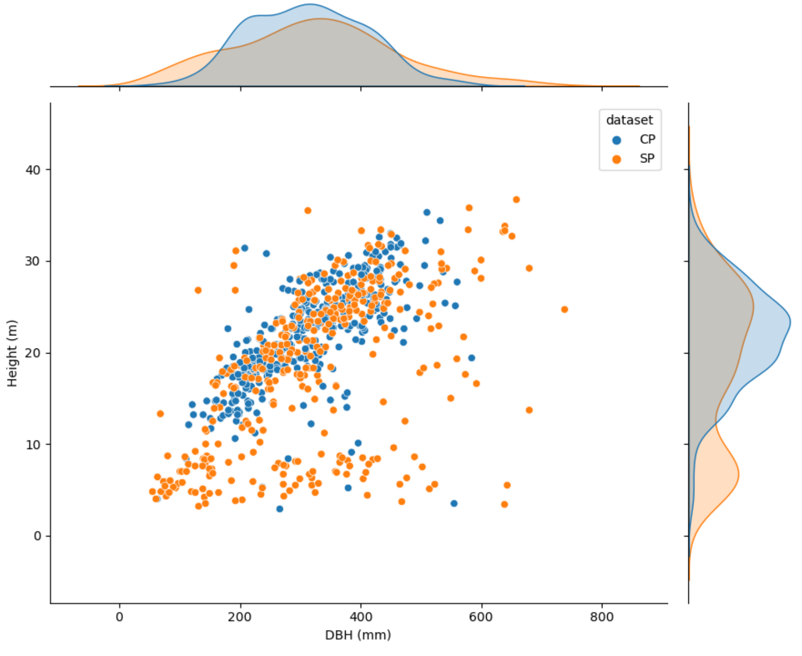

FIGURE 12 Joint distributions of diameter at breast-height (DBH) and tree height from field-based inventory data. It should be noted that the two datasets are differently distributed—i.e. there is a dataset shift [82] between sampling plots (SP) and control plots (CP) datasets.

Annex V: Elevation map of the study site

We provide the digital elevation model of the study area (Figure 13, a) to understand differences in flight heights (Figure 2) and to complement the information given on terrain exposure and surface hydrology (Figure 9). Figure 13, (b) shows the five rejected SP-plots and one valid (i.e. SP-18), for comparison. Among the rejected SP-plots, 1, 2, 9 and 10 show an insufficiently descriptive CHM, while SP-14 shows an intractable allocation of ground-based labels. All five rejected SP-plots were discarded before starting the modelling process, so they did not take part in the regression experiments.

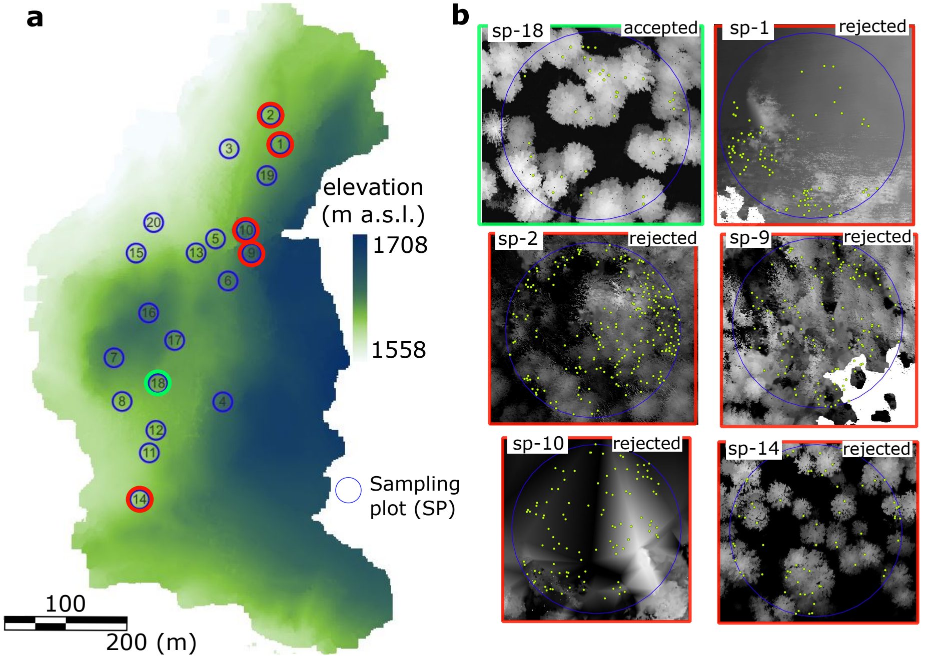

FIGURE 13 **a:** Digital elevation model of the stud area. a.s.l.: elevation above sea level, in m. The blue circles represent the SP-plots, numbered by their ID code (1-20). The green and red circles refer to the plots shown in panel b. **b:** Five SP-plots rejected and one valid (SP-18) given for comparison of contrasting quality of canopy height models, derived from the UAV-LiDAR point cloud data. In all six SP-plots, the yellow dots indicate the location of tree stems according to the field-based inventory.

Graphical Abstract

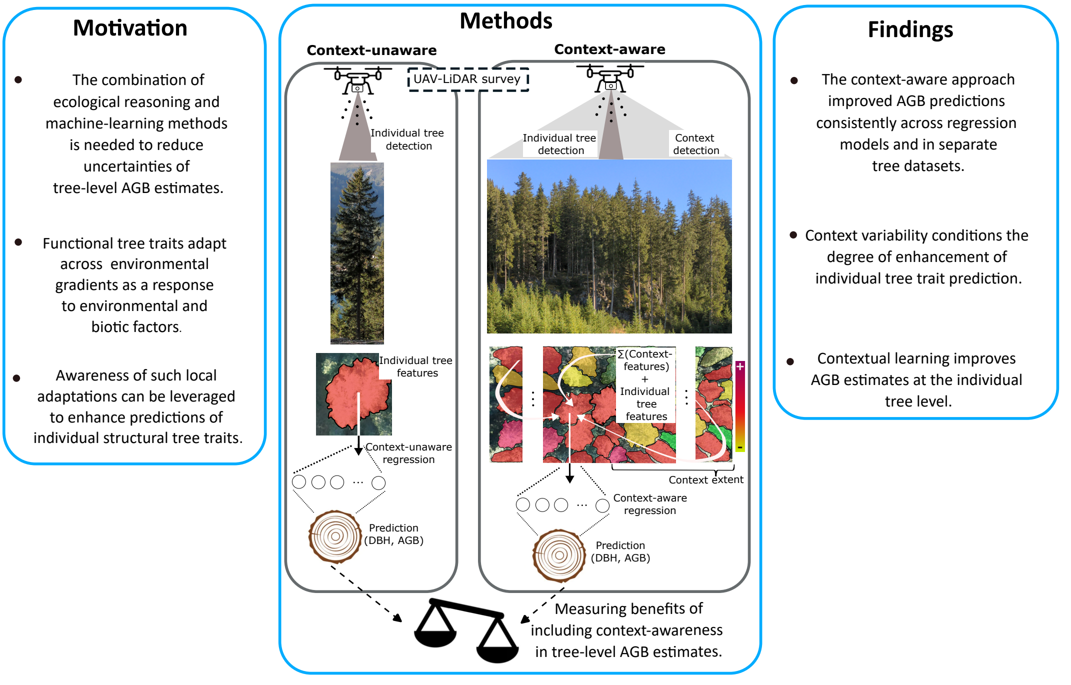

FIGURE 14 Graphical Abstract of the study.

References

[1] Fatichi S, Pappas C, Zscheischler J, Leuzinger S. Modelling carbon sources and sinks in terrestrial vegetation. New Phytologist 2019;221(2):652–668.

[2] Pörtner HO, Roberts DC, Adams H, Adler C, Aldunce P, Ali E, et al. Climate change 2022: Impacts, adaptation and vulnerability. IPCC Geneva, Switzerland:; 2022.

[3] Gundersen P, Thybring EE, Nord-Larsen T, Vesterdal L, Nadelhoffer KJ, Johannsen VK. Old-growth forest carbon sinks overestimated. Nature 2021;591(7851):E21–E23.

[4] Friedlingstein P, Jones MW, O'sullivan M, Andrew RM, Hauck J, Peters GP, et al. Global carbon budget 2019. Earth System Science Data 2019;11(4):1783–1838.

[5] Baccini A, Walker W, Carvalho L, Farina M, Sulla-Menashe D, Houghton R. Tropical forests are a net carbon source based on aboveground measurements of gain and loss. Science 2017;358(6360):230–234.

[6] Duncanson L, Armston J, Disney M, Avitabile V, Barbier N, Calders K, et al. The importance of consistent global forest aboveground biomass product validation. Surveys in geophysics 2019;40:979–999.

[7] Santini F, Kefauver SC, Resco de Dios V, Araus JL, Voltas J. Using unmanned aerial vehicle-based multispectral, RGB and thermal imagery for phenotyping of forest genetic trials: A case study in Pinus halepensis. Annals of Applied Biology 2019;174(2):262–276.

[8] Yao W, Krull J, Krzystek P, Heurich M. Sensitivity analysis of 3D individual tree detection from LiDAR point clouds of temperate forests. Forests 2014;5(6):1122–1142.

[9] Dalponte M, Coomes DA. Tree-centric mapping of forest carbon density from airborne laser scanning and hyperspectral data. Methods in ecology and evolution 2016;7(10):1236–1245.

[10] Kükenbrink D, Hueni A, Schneider FD, Damm A, Gastellu-Etchegorry JP, Schaepman ME, et al. Mapping the irradiance field of a single tree: Quantifying vegetation-induced adjacency effects. IEEE Transactions on Geoscience and Remote Sensing 2019;57(7):4994–5011.

[11] Cabo C, Ordóñez C, López-Sánchez CA, Armesto J. Automatic dendrometry: Tree detection, tree height and diameter estimation using terrestrial laser scanning. International journal of applied earth observation and geoinformation 2018;69:164–174.

[12] Kukkonen M, Maltamo M, Korhonen L, Packalen P. Multispectral airborne LiDAR data in the prediction of boreal tree species composition. IEEE Transactions on Geoscience and Remote Sensing 2019;57(6):3462–3471.

[13] Hao Y, Widagdo FRA, Liu X, Quan Y, Dong L, Li F. Individual tree diameter estimation in small-scale forest inventory using UAV laser scanning. Remote Sensing 2020;13(1):24.

[14] Yang Z, Liu Q, Luo P, Ye Q, Sharma RP, Duan G, et al. Nonlinear mixed-effects height to crown base model based on both airborne LiDAR and field datasets for Picea crassifolia Kom trees in northwest China. Forest Ecology and Management 2020;474:118323.

[15] Liu X, Hao Y, Widagdo FRA, Xie L, Dong L, Li F. Predicting height to crown base of Larix olgensis in Northeast China Using UAV-LiDAR data and nonlinear mixed effects models. Remote Sensing 2021;13(9):1834.

[16] Sun S, Cao QV, Cao T. Evaluation of distance-independent competition indices in predicting tree survival and diameter growth. Canadian Journal of Forest Research 2019;49(5):440–446.

[17] Zhang B, Sajjad S, Chen K, Zhou L, Zhang Y, Yong KK, et al. Predicting tree height-diameter relationship from relative competition levels using quantile regression models for Chinese fir (Cunninghamia lanceolata) in Fujian province, China. Forests 2020;11(2):183.

[18] Lo CS, Lin C. Growth-competition-based stem diameter and volume modeling for tree-level forest inventory using airborne LiDAR data. IEEE Transactions on Geoscience and Remote Sensing 2012;51(4):2216–2226.

[19] Potvin C, Dutilleul P. Neighborhood effects and size-asymmetric competition in a tree plantation varying in diversity. Ecology 2009;90(2):321–327.

[20] Ratcliffe S, Holzwarth F, Nadrowski K, Levick S, Wirth C. Tree neighbourhood matters–Tree species composition drives diversity–productivity patterns in a near-natural beech forest. Forest Ecology and Management 2015;335:225–234.

[21] Andersen HE, McGaughey RJ, Reutebuch SE. Estimating forest canopy fuel parameters using LIDAR data. Remote sensing of Environment 2005;94(4):441–449.

[22] Næsset E, Økland T. Estimating tree height and tree crown properties using airborne scanning laser in a boreal nature reserve. Remote Sensing of Environment 2002;79(1):105–115.

[23] Rijal B, Weiskittel AR, Kershaw Jr JA. Development of height to crown base models for thirteen tree species of the North American Acadian Region. The Forestry Chronicle 2012;88(1):60–73.

[24] Antonio N, Tome M, Tome J, Soares P, Fontes L. Effect of tree, stand, and site variables on the allometry of Eucalyptus globulus tree biomass. Canadian Journal of Forest Research 2007;37(5):895–906.

[25] Hyyppä E, Yu X, Kaartinen H, Hakala T, Kukko A, Vastaranta M, et al. Comparison of backpack, handheld, under-canopy UAV, and above-canopy UAV laser scanning for field reference data collection in boreal forests. Remote Sensing 2020;12(20):3327.

[26] Li N, Ho CP, Xue J, Lim LW, Chen G, Fu YH, et al. A Progress Review on Solid-State LiDAR and Nanophotonics-Based LiDAR Sensors. Laser & Photonics Reviews 2022;16(11):2100511.

[27] Oehmcke S, Li L, Revenga JC, Nord-Larsen T, Trepekli K, Gieseke F, et al. Deep learning based 3D point cloud regression for estimating forest biomass. In: Proceedings of the 30th International Conference on Advances in Geographic Information Systems; 2022. p. 1–4.

[28] Réjou-Méchain M, Barbier N, Couteron P, Ploton P, Vincent G, Herold M, et al. Upscaling forest biomass from field to satellite measurements: sources of errors and ways to reduce them. Surveys in Geophysics 2019;40(4):881–911.

[29] Xu D, Wang H, Xu W, Luan Z, Xu X. LiDAR applications to estimate forest biomass at individual tree scale: Opportunities, challenges and future perspectives. Forests 2021;12(5):550.

[30] Biging GS, Dobbertin M. Evaluation of competition indices in individual tree growth models. Forest science 1995;41(2):360–377.

[31] Schiefer F, Kattenborn T, Frick A, Frey J, Schall P, Koch B, et al. Mapping forest tree species in high resolution UAV-based RGB-imagery by means of convolutional neural networks. ISPRS Journal of Photogrammetry and Remote Sensing 2020;170:205–215.

[32] Marques O, Barenholtz E, Charvillat V. Context modeling in computer vision: techniques, implications, and applications. Multimedia Tools and Applications 2011;51:303–339.

[33] Zhao R, Ouyang W, Li H, Wang X. Saliency Detection by Multi-Context Deep Learning. In: Proceedings of the IEEE Conference on Computer Vision and Pattern Recognition (CVPR); 2015. p. 1265–1274.

[34] Chu HJ, Wu CF, Lin YP. Incorporating spatial autocorrelation with neural networks in empirical land-use change models. Environment and Planning B: Planning and Design 2013;40(3):384–404.

[35] Luo W, Li Y, Urtasun R, Zemel R. Understanding the effective receptive field in deep convolutional neural networks. Advances in neural information processing systems 2016;29.

[36] Yang W, Tan RT, Feng J, Liu J, Guo Z, Yan S. Deep joint rain detection and removal from a single image. In: Proceedings of the IEEE conference on computer vision and pattern recognition; 2017. p. 1357–1366.

[37] Liu YF, Jaw DW, Huang SC, Hwang JN. DesnowNet: Context-aware deep network for snow removal. IEEE Transactions on Image Processing 2018;27(6):3064–3073.

[38] Heiskanen J, C B, N B, C C, H C, B G, et al. The Integrated Carbon Observation System in Europe. Bulletin of the American Meteorological Society 2022;103(3):E855–E872.

[39] Juszczak T. Voluntary National report to UNF1 from Switzerland. United Nations, Department of Ecoomic and Social Affairs - Forests; 2019.

[40] Burri S. Long-Term Environmental Research–The Davos-Seehornwald Site. ETH Zurich Research collection 2019;.

[41] WSL. Long-term Forest Ecosystem Research (WSL); 2023.

[42] TreeNet. Biological drought and growth indicator network; 2023.

[43] ETH-Zurich. Biological drought and growth indicator network; 2023.

[44] ICOS. Integrated Carbon Observation System; 2023.

[45] ICP-Forest. International Co-operative Programme on Assessment and Monitoring of Air Pollution Effects on Forests; 2023.

[46] eLTER. Integrated European Long-Term Ecosystem, critical zone and socio-ecological Research; 2023.

[47] Revenga JC, Trepekli K, Oehmcke S, Jensen R, Li L, Igel C, et al. Above-Ground Biomass Prediction for Croplands at a Sub-Meter Resolution Using UAV–LiDAR and Machine Learning Methods. Remote Sensing 2022;14(16):3912.

[48] Davidson L, Mills J, Haynes I, Augarde C, Bryan P, Douglas M. Airborne to UAS LiDAR: An analysis of UAS LiDAR ground control targets. ISPRS Geospatial Week 2019;.

[49] Swiss Federal Institute for Forest S, (WSL) LR. Methods of the Sanasilva Inventory; 2023.

[50] Hunziker S, Begert M, Scherrer SC, Rigling A, Gessler A. Below average midsummer to early autumn precipitation evolved into the main driver of sudden Scots pine vitality decline in the Swiss Rhône valley. Frontiers in Forests and Global Change 2022;p. 103.

[51] ICOS-ETC. Instruction on ancillary vegetation measurements in forest; 2023.

[52] Chen Q GP Baldocchi D, M K. Isolating Individual Trees in a Savanna Woodland Using Small Footprint Lidar Data. In: Photogrammetric Engineering and Remote Sensing, 72(8): 923-932; 2006. p. 923–932.

[53] GreenValley-International. LiDAR360 User Guide. California, USA; January 2021, www.greenvalletintl.com.

[54] Anselin L. Local indicators of spatial association—LISA. Geographical analysis 1995;27(2):93–115.

[55] Anselin L, Rey SJ. Perspectives on spatial data analysis. In: Perspectives on spatial data analysis Springer; 2010.p. 1–20.

[56] Breunig MM, Kriegel HP, Ng RT, Sander J. LOF: identifying density-based local outliers. In: Proceedings of the 2000 ACM SIGMOD international conference on Management of data; 2000. p. 93–104.

[57] Liu FT, Ting KM, Zhou ZH. Isolation forest. In: 2008 eighth ieee international conference on data mining IEEE; 2008. p. 413–422.

[58] Anselin L, Syabri I, Kho Y. GeoDa: an introduction to spatial data analysis. In: Handbook of applied spatial analysis: Software tools, methods and applications Springer; 2009.p. 73–89.

[59] Da Silva BC, Basso EW, Bazzan AL, Engel PM. Dealing with non-stationary environments using context detection. In: Proceedings of the 23rd international conference on Machine learning; 2006. p. 217–224.

[60] Fu WJ, Jiang PK, Zhou GM, Zhao KL. Using Moran's I and GIS to study the spatial pattern of forest litter carbon density in a subtropical region of southeastern China. Biogeosciences 2014;11(8):2401–2409.

[61] Cressie N. Statistics for spatial data. John Wiley & Sons; 2015.

[62] Getis A, Ord JK. The analysis of spatial association by use of distance statistics. In: Perspectives on spatial data analysis Springer; 2010.p. 127–145.

[63] Westerholt R, Resch B, Mocnik FB, Hoffmeister D. A statistical test on the local effects of spatially structured variance. International Journal of Geographical Information Science 2018;32(3):571–600.

[64] Hastie TJ. Generalized additive models. In: Statistical models in S Routledge; 2017.p. 249–307.

[65] Anselin L, et al. Spatial econometrics. A companion to theoretical econometrics 2001;310330.

[66] Beven KJ, Kirkby MJ. A physically based, variable contributing area model of basin hydrology/Un modèle à base physique de zone d'appel variable de l'hydrologie du bassin versant. Hydrological sciences journal 1979;24(1):43–69.

[67] Mohamedou C, Tokola T, Eerikäinen K. LiDAR-based TWI and terrain attributes in improving parametric predictor for tree growth in southeast Finland. International journal of applied earth observation and geoinformation 2017;62:183–191.

[68] Kopecký M, Macek M, Wild J. Topographic Wetness Index calculation guidelines based on measured soil moisture and plant species composition. Science of the Total Environment 2021;757:143785.

[69] ESRI. ArcGis Pro: Implementation Guide. Redlands, California; 2021, www.esri.com.

[70] Landini G. Particles8 class: An ImageJ plugin for estimating various statistics of binary 8- connected particles.; 2010.

[71] Güler C, Beyhan B, Tağa H. PolyMorph-2D: An open-source GIS plug-in for morphometric analysis of vector-based 2D polygon features. Geomorphology 2021;386:107755.

[72] Steiniger S, Blake L. OpenJUMP software; 2022.

[73] Freund Y, Schapire RE. A decision-theoretic generalization of on-line learning and an application to boosting. Journal of computer and system sciences 1997;55(1):119–139.

[74] Friedman JH. Greedy function approximation: a gradient boosting machine. Annals of statistics 2001;p. 1189–1232.

[75] Schapire RE. Explaining adaboost. Empirical Inference: Festschrift in Honor of Vladimir N Vapnik 2013;p. 37–52.

[76] Tibshirani R. Regression shrinkage and selection via the lasso. Journal of the Royal Statistical Society: Series B (Methodological) 1996;58(1):267–288.

[77] Ho TK. Random decision forests. In: Proceedings of 3rd international conference on document analysis and recognition, vol. 1 IEEE; 1995. p. 278–282.

[78] Vidaurre D, Bielza C, Larranaga P. A survey of L1 regression. International Statistical Review 2013;81(3):361–387.

[79] Demol M, Verbeeck H, Gielen B, Armston J, Burt A, Disney M, et al. Estimating forest above-ground biomass with terrestrial laser scanning: Current status and future directions. Methods in Ecology and Evolution 2022;13(8):1628–1639.

[80] Gryc V, Horáček P. Variability in density of spruce (Picea abies [L.] Karst.) wood with the presence of reaction wood. Journal of forest science 2007;53(3):129–137.

[81] Scrinzi G, Galvagni D, Marzullo L. I nuovi modelli dendrometrici per la stima delle masse assestamentali in Provincia di Trento. Provincia autonoma di Trento. Servizio foreste e fauna; 2010.

[82] Quionero-Candela J, Sugiyama M, Schwaighofer A, Lawrence ND. Data Set Shift in Machine Learning. MIT Press, Cambridge, Massachusetts; 2009. http://www.acad.bg/ebook/ml/The.MIT.Press.Dataset.Shift.in.Machine.Learning.Feb.2009.eBook-DDU.pdf.

[83] Bates S, Hastie T, Tibshirani R. Cross-validation: what does it estimate and how well does it do it? arXiv preprint arXiv:210400673 2021;.

[84] Altmann A, Toloşi L, Sander O, Lengauer T. Permutation importance: a corrected feature importance measure. Bioinformatics 2010;26(10):1340–1347.

[85] Wilcoxon F. Individual comparisons by ranking methods. Springer; 1992.

[86] Cliff N. Dominance statistics: Ordinal analyses to answer ordinal questions. Psychological bulletin 1993;114(3):494.

[87] Horton RE. Drainage-basin characteristics. Transactions, American geophysical union 1932;13(1):350–361.

[88] Zingg T. Beitrag zur schotteranalyse. PhD thesis, ETH Zurich; 1935.

[89] Buendıa P, Soler C, Paolicchi F, Gago G, Urquieta B, Pérez-Sánchez F, et al. Morphometric characterization and classification of alpaca sperm heads using the Sperm-Class Analyzer® computer-assisted system. Theriogenology 2002;57(4):1207–1218.

[90] Attneave F, Arnoult MD. The quantitative study of shape and pattern perception. Psychological bulletin 1956;53(6):452.

[91] Zăvoianu I. Morfometria bazinelor hidrografice. Editura Academiei Republicii Socialiste România; 1978.

[92] Miller VC. A QUANTITATIVE GEOMORPHIC STUDY OF DRAINAGE BASIN CHARACTERISTICS IN THE CLINCH MOUNTAIN AREA VIRGINIA AND TENNESSEE. Columbia Univ New York; 1953.

[93] Schumm SA. Evolution of drainage systems and slopes in badlands at Perth Amboy, New Jersey. Geological society of America bulletin 1956;67(5):597–646.

[94] Chorley RJ, Malm E Donald E, Pogorzelski HA. A new standard for estmating drainage basin shape. American Journal of Science 1957;255:138–141.

[95] Horgan GW, Glasbey CA. Uses of digital image analysis in electrophoresis. Electrophoresis 1995;16(1):298–305.

[96] Zunic J, Rosin PL. A new convexity measure for polygons. IEEE Transactions on Pattern Analysis and Machine Intelligence 2004;26(7):923–934.

[97] Rosin PL. Measuring rectangularity. Machine Vision and Applications 1999;11:191–196.

[98] Wadell H. Volume, shape, and roundness of quartz particles. The Journal of Geology 1935;43(3):250–280.

[99] Valladares F, Arrieta S, Aranda I, Lorenzo D, Sánchez-Gómez D, Tena D, et al. Shade tolerance, photoinhibition sensitivity and phenotypic plasticity of Ilex aquifolium in continental Mediterranean sites. Tree physiology 2005;25(8):1041–1052.

[100] Valladares F, Dobarro I, Sánchez-Gomez D, Pearcy RW. Photoinhibition and drought in Mediterranean woody saplings: scaling effects and interactions in sun and shade phenotypes. Journal of Experimental Botany 2005;56(411):483–494.

[101] Pillar VD, Duarte LdS, Sosinski EE, Joner F. Discriminating trait-convergence and trait-divergence assembly patterns in ecological community gradients. Journal of Vegetation Science 2009;20(2):334–348.

[102] Naesset E. Determination of mean tree height of forest stands using airborne laser scanner data. ISPRS Journal of Photogrammetry and Remote sensing 1997;52(2):49–56.

[103] Guillén-Escribà C, Schneider FD, Schmid B, Tedder A, Morsdorf F, Furrer R, et al. Remotely sensed between-individual functional trait variation in a temperate forest. Ecology and Evolution 2021;11(16):10834–10867.

[104] Zheng Z, Zeng Y, Schuman MC, Jiang H, Schmid B, Schaepman ME, et al. Individual tree-based vs pixel-based approaches to mapping forest functional traits and diversity by remote sensing. International Journal of Applied Earth Observation and Geoinformation 2022;114:103074.

[105] Wang CJ, Zhang ZX, Wan JZ. Vulnerability of global forest ecoregions to future climate change. Global Ecology and Conservation 2019;20:e00760.

[106] He X, Zemel RS, Carreira-Perpinán MA. Multiscale conditional random fields for image labeling. In: Proceedings of the 2004 IEEE Computer Society Conference on Computer Vision and Pattern Recognition, 2004. CVPR 2004., vol. 2 IEEE; 2004. p. II–II.

[107] Yu F, Koltun V. Multi-scale context aggregation by dilated convolutions. arXiv preprint arXiv:151107122 2015;.

[108] Abelleira Martínez OJ, Fremier AK, Günter S, Ramos Bendaña Z, Vierling L, Galbraith SM, et al. Scaling up functional traits for ecosystem services with remote sensing: concepts and methods. Ecology and Evolution 2016;6(13):4359–4371.

[109] Ma X, Migliavacca M, Wirth C, Bohn FJ, Huth A, Richter R, et al. Monitoring plant functional diversity using the reflectance and echo from space. Remote Sensing 2020;12(8):1248.

[110] Goebes P, Schmidt K, Seitz S, Both S, Bruelheide H, Erfmeier A, et al. The strength of soil-plant interactions under forest is related to a Critical Soil Depth. Scientific Reports 2019;9(1):8635.

[111] Green JK, Keenan TF. The limits of forest carbon sequestration. Science 2022;376(6594):692–693.

[112] Valladares F, Gianoli E, Gómez JM. Ecological limits to plant phenotypic plasticity. New phytologist 2007;176(4):749–763.

[113] Kraft NJ, Adler PB, Godoy O, James EC, Fuller S, Levine JM. Community assembly, coexistence and the environmental filtering metaphor. Functional ecology 2015;29(5):592–599.

[114] Strahler AN. Hypsometric (area-altitude) analysis of erosional topography. Geological society of America bulletin 1952;63(11):1117–1142.

[115] Berrar D. Cross-Validation. Encyclopedia of Bioinformatics and Computational Biology 2018;1:542–545.